Two ways of suppressing charge density waves in $1T$-$TiSe_2$

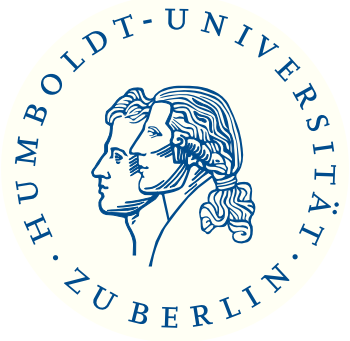

Diplomarbeit

Humboldt-Universität zu Berlin
Mathematisch-Naturwissenschaftliche Fakultät I
Institut für Physik

eingereicht von

Matthias M. May

Berlin, den 06.09.2010

Contents

1 Introduction

Charge density waves (CDWs) represent a fundamental collective phenomenon in solids, similar to high-temperature superconductors. In principle, the distribution of charges in a solid is given by the regular arrangement of its atoms, the crystal structure. With the onset of a charge density wave, this distribution undergoes a change and forms a periodical superstructure, which can be detected with different experimental methods like photoelectron spectroscopy (PES) or low energy electron diffraction (LEED). This superstructure in the charge distribution is usually accompanied by a periodical lattice distortion of the crystal lattice. Typically, this phase transition appears below a critical temperature T_c but as it is a phase transition of second order, the CDW forms rather gradually than abrupt.

Apart from the general interest in fundamental effects in solids, CDWs are also a subject of research due to their close relationship to superconductivity. This is a phenomenon that has - unlike CDWs - already found many applications, e.g. where high magnetic fields are needed as in medicine like magnetic resonance imaging units. Originally, CDWs were proposed as an explanation for superconductivity [1]. Later, excitons were believed to be a way towards 'non-phonon' room temperature superconductors [2] as the 'glue' of electron-electron pairs, but this has proven wrong until now due to the development of CDWs that prevent the use of excitons for pair formation. Hence the close relationship of those two phenomena is well established, often competing in the same material [3].

Among the layered transition metal dichalcogenides (TMDCs) ranging from metals to insulators, many materials can be found that show a superconducting phase, a CDW phase or both. $TiSe_2$ shows both phases and its semiconducting nature has just been established [4] evidencing the smallest - 150 meV - band gap of the TMDCs. Further members of the family are the semiconductor TiS_2 and the semimetal $TiTe_2$. Their structural and electronic relationships allow to tune the band gap by *band gap engineering* when growing ternary crystals $TiSe_{2-x}S_x/Te_x$. Their layered structure is very advantageous for adsorption experiments as surfaces without dangling bonds can be produced. This allows to change the population of bands on the surface by band-bending induced by H_2O adsorption.

The driving force of this phase transition - at least in the studied material $TiSe_2$ - is still under discussion although $TiSe_2$ was one of the first materials where a CDW phase transition was found by `Di Salvo et al` in 1976 [5]. Three main models were proposed to explain the CDW transition: *Fermi nesting, Jahn-Teller effect* and the *excitonic con-*

densate phase model. The latter is similar to the BCS theory in superconductors, where the superconducting phase is driven by the formation of electron-electron pairs, so called Cooper-pairs. This thesis tries to find evidence which model to prefer by exterior influence, namely water adsorption, and interior influence by changing the stoichiometry with the main experimental focus lying on photoelectron spectroscopy.

In chapter 2 $TiSe_2$ will be introduced and an overview over charge density waves will be given. The third chapter will outline the experimental techniques used in the present work. The results will be presented and discussed in chapter 4, while the summary will conclude in chapter 5.

2 Background

Charge density waves have already been a subject of interest for a long time with $TiSe_2$ as one of the first materials where a CDW phase was discovered [5]. To get a better understanding why a CDW phase can occur in $TiSe_2$ and which model explaining its driving fits best, an understanding of its structure is essential. This chapter will first introduce the transition metal dichalcogenide $TiSe_2$ regarding the crystal and electronic structure. The second part is dedicated to the theoretical description of the charge density wave phase transition with a sketch of the different models.

2.1 $TiSe_2$ - a transition metal dichalcogenide

The family of the TMDCs forming TX_2 is composed of the transition metals (groups 3-12 of the periodic table) T like titanium or zirconium and chalcogenides (group 16) X like selenium, sulphur or tellurium. The most well-known TMDC is probably MoS_2 which has found an application as solid lubricant. Promising for photovoltaics is e.g. zirconium disulfide (ZrS_2) which is a subject of active research in HU group EES [6]. The TMDCs typically grow in layered crystals similar to graphite. Their electronic properties range from metals like VSe_2 to insulators like HfS_2 [7].
The TMDC studied here is titanium diselenide ($TiSe_2$) and two compounds derived from it, TiS_xSe_{2-x} and $TiTe_xSe_{2-x}$. The latter were chosen as TiS_2 and $TiTe_2$ are also members of the TMDC family having very similar crystal and electronic structures but a bigger band gap for TiS_s and a band overlap for $TiTe_2$. $TiSe_2$ is a very interesting subject studying CDWs, as it is a semiconductor with a very small band gap [8] allowing to investigate the necessity of a positive or negative band gap for the phase transition by tuning the band gap size with *band gap engineering* described later in this section. Additionally, its crystal structure makes physisorption experiments possible, since it does not have dangling bonds in the c direction - (001) surface - which could react with the adsorbed molecules.

2.1.1 Crystal structure

The TMDCs considered here form a CdI_2-type crystal structure where one transition metal atom is coordinated by six chalcogen atoms (fig. 2.1a). The two existing polytypes $1T$ and $2H$ share an X-T-X sequence of the atomic layers where the bonding is covalent-ionic. In the $2H$ polytype the coordination of the T atoms is trigonal prismatic and two

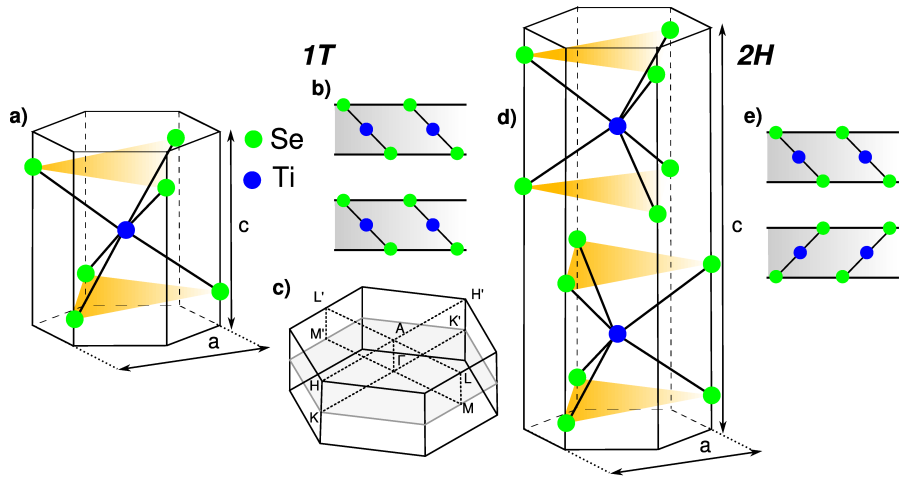

Figure 2.1: a) Unit cell of the $1T$ polytype on the example of $TiSe_2$, b) layered structure for $1T$ with van der Waals gap, c) Brillouin zone of $1T$ d) unit cell of $2H$, e) layered structure for $2H$.

consecutive layers are rotated 60 ° around the c axis. Therefore two slabs are needed to form a unit cell which has hexagonal rotation symmetry, hence the term $2H$. For the $1T$ polytype, the coordination of the T atoms is octahedral and only one layer is needed for the unit cell leading to a trigonal rotation symmetry, $1T$. The bonding between the layers (fig. 2.1b) is of the weak van der Waals type. This aspect of the structure is the origin of a common feature in TMDCs [9] called *intercalation*, where e.g. non-stoichiometric atoms from crystal growth can be incorporated between the layers in the van der Waals gap. $TiSe_2$ only crystallises in the $1T$ polytype with a trigonal distortion of the ideal octahedral coordination leading to bigger atomic distances in the c direction. This is also true for TiS_2 and $TiTe_2$. The lattice constants as well as the important parameters $c^* = \frac{2\pi}{c}$ and $\Gamma\mathrm{M} = \frac{b}{2} = \frac{4\pi}{2a\sqrt{3}}$ are given in table 2.1.

Material	a / Å	c / Å	c^* / Å^{-1}	ΓM / Å^{-1}
$TiSe_2$	3.537	6.00	1.047	1.026
TiS_2	3.405	5.687	1.105	1.065
$TiTe_2$	3.773	6.516	0.964	0.916

Table 2.1: Crystal parameters for the three materials [10].

The primitive real space cell and the Brillouin zone have the same orientation, which simplifies orientation for well-grown crystals.

Symmetry Though the points L'(M') and L(M) are equivalent by symmetry, the contents of the the rectangles ΓAL'M' and ΓALM are not (see fig. 2.1a) and c)). This means, that the band structure would only be equivalent, if the bands in k_z direction were perfectly flat as discussed e.g. in [11]. This flatness is only a good approximation of first order, as this can be seen e.g. in Fermi maps by `Thürmer` [12] where the Fermi surface differs for L and L'.

2.1.2 Electronic structure

As a member of group 4 in the periodic table of elements, the electron configuration of Ti is $[\mathrm{Ar}]4s^2 3d^2$, while the group 16 elements S, Se and Te have a $[\mathrm{Ne}]3s^2 3p^4$, $[\mathrm{Ar}]4s^2 3d^{10} 4p^4$ and $[\mathrm{Kr}]5s^2 4d^{10} 5p^4$ configuration, respectively. According to `Kim et al.` [14, 13], the valence bands in TiX_2 mainly consist of the calcogen's orbitals, the ns ($n = 3, 4, 5$ respectively for X=S, Se and Te) labelled a in fig. 2.2 and the three np bands (peaks b_1, b_2, b_3 in fig. 2.2). Indicating a strong covalent bonding, these states also contain components of Ti orbitals, the sum over all contributions in fig. 2.2 is drawn in red. The conduction band above E_F mainly consists of the Ti $3d$ band with the peaks indexed c_1 and c_2 in fig. 2.2. Due to the octahedral ligand field, the Ti $3d$ band splits into a twice degenerated e_g doublet with higher energy and a degenerated triplet t_{2g} at lower energy. Above Ti $3d$ the anti-bonding $4sp$ orbital can be found. As the energy of the Ti $3d$ e_g orbital lies much higher than the t_{2g} orbital, it will not be considered here. The main focus of this thesis lies on the the Ti $3d$ t_{2g} and Se $4p$ orbitals. Note that fig. 2.2 sees $TiSe_2$ as a semimetal, which is believed to be a wrong assumption.

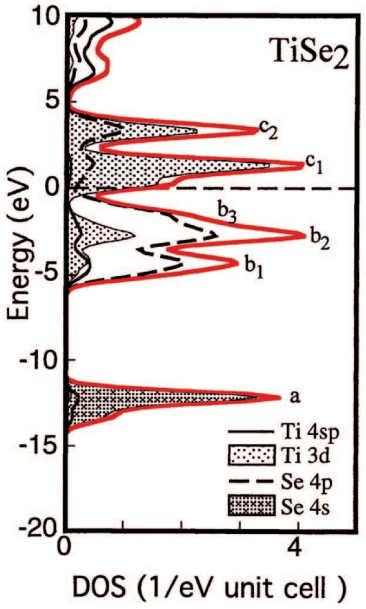

Figure 2.2: Densitiy of states for $TiSe_2$ from from `Kim et al.` [13], explanation see text.

The electronic structure of $TiSe_2$ is still subject of discussion. The subject of the discussion is, whether $TiSe_2$ can be described as a semimetal or a semiconductor. The difference between a metal and a semimetal is the Fermi level lying very close to the upper end of the valence band or the lower part of the conduction band for the semimetal

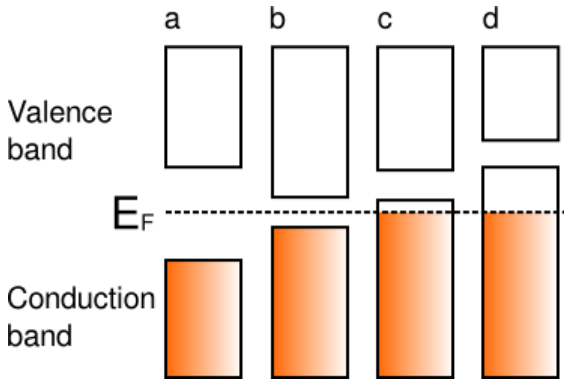

Figure 2.3: Definition of a) insulator wit big energy gap b) semiconductor with smaller energy gap c) semimetal with E_F slightly within a band d) metal with E_F deeper in a band. Occupied states below Fermi level E_F in orange.

(see fig. 2.3), which results in a reduced conductivity. By now, most sources agree that the absolute value - be it negative or positive - of the band gap is 150 meV or less [15]. In this work, $TiSe_2$ is considered a semiconductor according to previous water adsorption measurements by `Rasch et al.` [4] and `Thürmer` [12] realized in HU group EES evidencing a band gap of 150 meV. A calculated band structure by `Zunger et al.` [16] (fig. 2.4) shows the band structure derived theoretically from local-density approximation calculations, though with a band overlap. The maximum of the valence band can be found at Γ, while the minimum of the conduction band is located at the BZ boundary L. This results in a very indirect band gap. According to `Rasch et al.` [4], the dispersion of the uppermost valence band is of $O(40)$ meV between Γ and A. Additional calculations of DOS and band structures have been done e.g. by `Wezel et al.` [15], `Bullet` [17] and `Reshak et al.` [18]. It has to be added, that the theoretical determination of the size of a band gap with the currently available methods is inaccurate as absolute energies are difficult to determine. So it usually is adapted to experimental results.

2.1.3 Ternary compounds and band gap engineering

In table 2.1, the very similar crystal parameters of the TMDCs TiS_2, $TiSe_2$ and $TiTe_2$ were shown. The electronic structures are very alike as well, the relative position of the valence and conduction band is the main relevant difference here. While $TiTe_2$ is a semimetal with a band overlap also referenced as negative gap, $TiSe_2$ is a small-gap semiconductor and TiS_2 a semiconductor with a bigger gap. Similar to $TiSe_2$, there exist conflicting results about the nature of the band gap for TiS_2. While theoretical calculations range from semi-metal [18] to a gap of 2 eV [19], experimental results also indicate semi-metallic [20] or semiconducting [21] behaviour. In the work of `Thürmer`

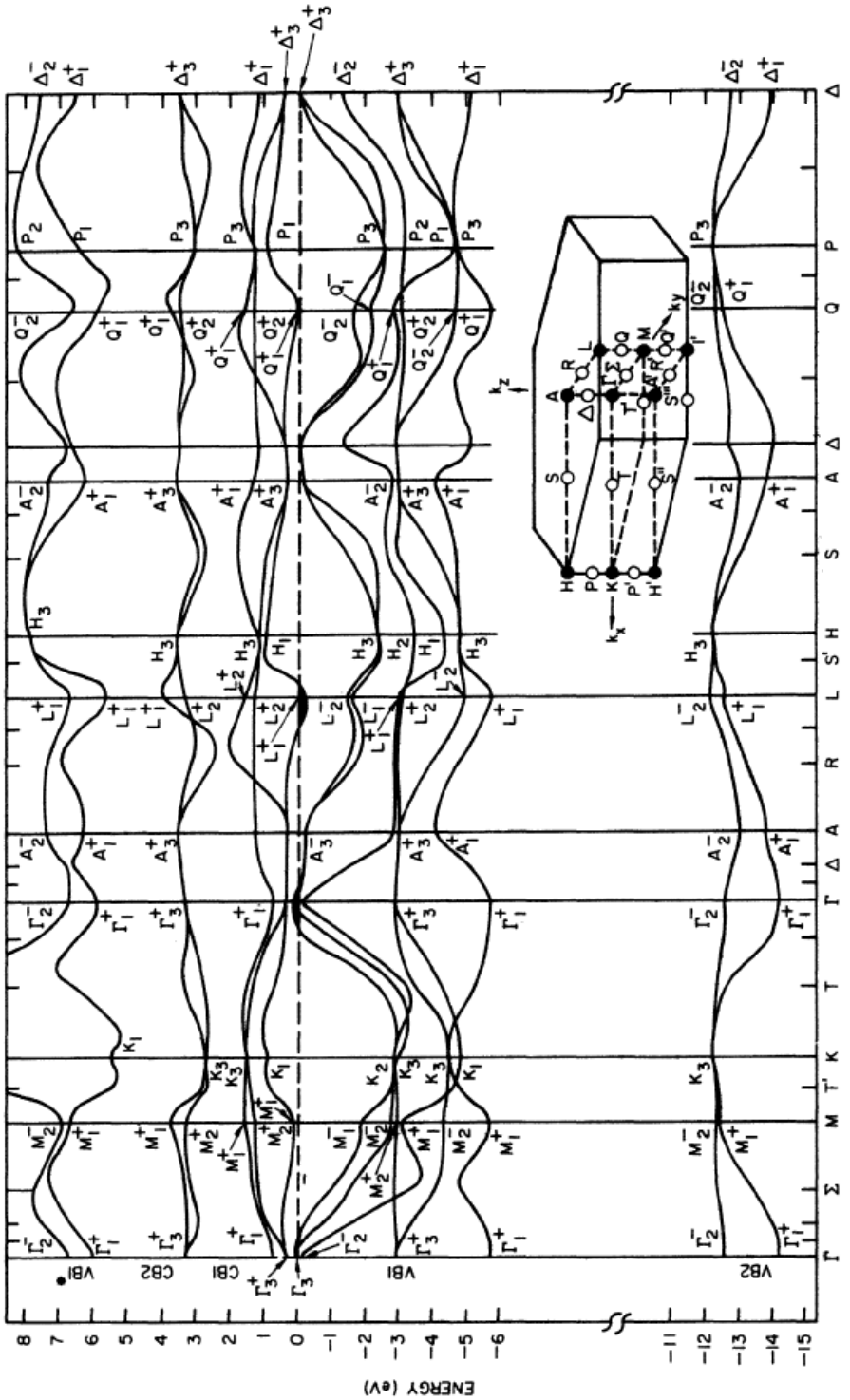

Figure 2.4: Calculated band structure for $TiSe_2$ by Zunger et al. [16].

[12] TiS_2 is found to be a semiconductor, yet he did not determine the exact size of the band gap. So the experimental value of 0.3 eV from `Chen et al.` [21] will be used here though this is considered as a lower bound. The nature of $TiTe_2$ is clearly semi-metallic with an overlap of 0.8 eV according to `Claessen et al.` [22].

Changing the band gap of a semiconductor by altering its stoichiometric composition is called **band gap engineering**. From using this method applied on the ternary TMDC ZrS_xSe_{2-x} by `Moustafa et al.` [23], the gap size can be approximated in first order to grow linearly with increasing x for ZrS_xSe_{2-x}. Using *band gap engineering* within the present work, the band gap of $TiSe_2$ was tuned to investigate the influence of its magnitude onto the CDW phase transition: TiS_2 is a semiconductor with a bigger band gap, therfore the resulting band gap of the ternary compound TiS_xSe_{2-x} is expected to increase with x. As $TiTe_2$ is a semimetal, the band gap of the ternary $TiTe_xSe_{2-x}$ should decrease with x. This is illustrated by a linear interpolation in fig. 2.5. According to `Bullet` [17], the band gap is sensitive to the electronegativity of the elements. While the electronegativity of S and Se is with $\chi = 2.6$ [24] very similar, the value for Te is $\chi = 2.1$. This could explain the different slopes of the band gap size as a function of the stoichiometric factor x.

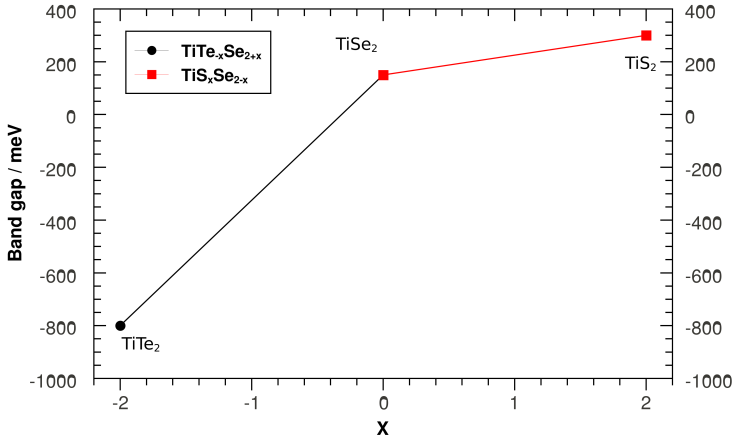

Figure 2.5: Linear interpolation of the band gap of ternary compounds as a function of x. For $TiTe_xSe_{2-x}$, the sign of x is inverted, a negative band gap indicates an overlap. Values for gap size from [22, 4, 21].

2.2 Charge density waves

The first neutron-diffraction studies in combination with resistivity measurements revealing the phase transition in $TiSe_2$ were already published in 1976 by `Di Salvo et`

al. [5], while Thompson mentioned an occurrence in $TiSe_2$ in 1975 [25]. Some other TMDCs also show CDW phase transitions as their low dimensionality favours CDWs, see [26] for a detailed review. However, neither TiS_2 nor $TiTe_2$ which are important for the understanding of the ternary compounds, show a CDW phase. In some high temperature superconductors this phenomenon appears as well, sometimes in combination with spin density waves. This close relation to superconductivity was even more emphasized by the discovery of a competing superconducting state in $TiSe_2$ induced by pressure [27] or Cu intercalation [3].

Different models for the explanation of CDW formations exist, but the applicability depends on the material. The most common one is **Fermi surface nesting**, though most sources agree that this does not apply for $TiSe_2$. The two other options discussed at present are a **Jahn-Teller effect** [28] or an **excitonic** origin [5, 29]. The latter is favoured due to the experimental results presented in chapter 4 and therefore will be applied to $TiSe_2$.

In this section, some characteristics of the CDW phase transition will be given before the first, basic model of CDWs, the Peierls transition, will be sketched. Furthermore, the two most promising models for $TiSe_2$ will be introduced and finally applied to the case of $TiSe_2$.

2.2.1 Characteristics

So what exactly is a charge density wave? In few words, it is a periodical modulation of the density of charge carriers usually associated with a structural phase transition of the crystal lattice, resulting in a periodical lattice distortion (PLD). This phase transition occurs below a critical temperature T_c. If the ratio a'/a of the PLD's lattice constant a' and the original structure, a, is an integer, it is called a *commensurate* CDW, otherwise an *incommensurate* CDW. The principle of a one-dimensional CDW with doubled periodicity is sketched in fig. 2.6, the two-dimensional case is depicted in fig. 2.7: Above T_c, the interatomic distance is a. Below T_c, two adjacent atoms approach and an additional symmetry with double periodicity is introduced.

2.2.2 Models

Three main models exist to explain the driving force of the CDW phase transition. While the **Peierls transition** is the oldest one, a **Jahn-Teller effect** or an **excitonic** origin are the models favoured for $TiSe_2$ by most research groups at present.

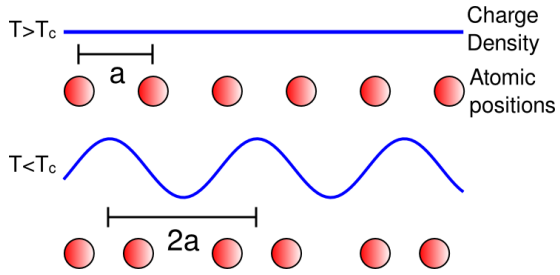

Figure 2.6: CDW in one dimension above and below critical temperature T_c with lattice constant a adapted from [30].

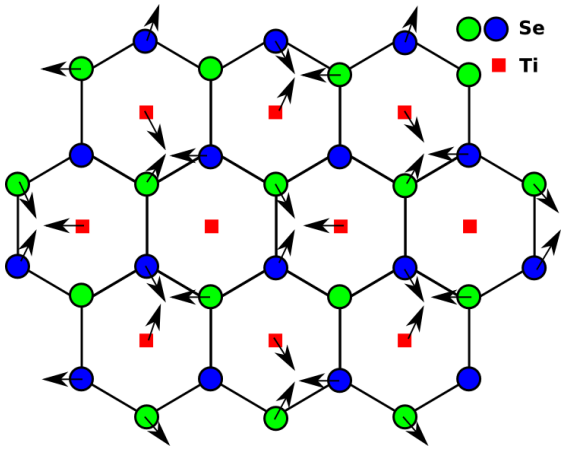

Figure 2.7: Periodical 2x2 lattice distortion in 2 dimensions.

Peierls transition

This basic model will be given here as it illustrates the concept of a CDW phase very nicely. The starting point is a one-dimensional monovalent metal exhibiting a half-filled conduction band with a homogeneous charge density. If its periodicity is doubled by a modulation of the charge density (fig. 2.6), the Brillouin zone will be cut in half and the energy at its edge near the vector $\vec{k_f}$ will be lowered opening a gap 2Δ (see fig. 2.8), like for the situation for a free electron gas in a periodical potential. If the energy needed for the lattice distortion is smaller than the energy gain, the overall energy can be lowered by this transition. So the preferred ground state at sufficiently low temperatures becomes the CDW phase and an excitation energy of at least 2Δ ist needed to allow conduction. This metal-insulator transition is also called **Peierls transition** after `Peierls` stating this possibility in 1930 [31]. For a one-dimensional metal the Fermi surface consists of parallel planes separated by the vector $2\vec{k_f}$ so there is a large number

of Umklapp scattering with the nesting vector $\vec{Q} = 2\vec{k_f}$. In a two-dimensional metal the Fermi surface is a cylinder so the parallel portions become lines and in three dimensions points. This is the reason why low-dimensional materials are good candidates for Fermi nesting. However, Fermi nesting does not apply for $TiSe_2$ due to the topology of its Fermi surface not showing large parallel components.

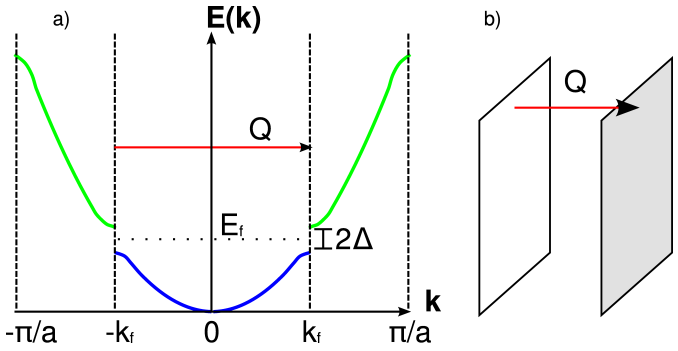

Figure 2.8: a) Development of the energy gap 2Δ in the Peierls transition, blue indicating occupied states, green unoccupied states, Fermi momentum $\vec{k_f}$ and Fermi energy E_f, nesting vector Q b) 1D case of nesting with parallel Fermi surface.

Band-type Jahn-Teller effect

The **band-type Jahn Teller** explanation of the CDW phase in $TiSe_2$ was originally proposed by `Hughes` in 1977 [28] and recently defended by `Rossnagel et al.` [32]. In this model the overall energy of the system is lowered by a structural transition from the local octahedral $1T$ coordination towards trigonal prismatic $2H$: The upper and lower faces of the selenium octahedra are rotated in opposite directions (see fig. 2.7). This leads to a symmetry break, the degeneration of the t_{2g} triplet lifted a shift of the Ti $3d$ band towards lower energies. The structural transition of creates a periodical lattice distortion which then gives rise to the periodical modulation of the charge density, the CDW. But, as `Hughes` notes, the "Jahn-Teller mechanism of course relies on the partial occupation of the lowest d-band" [28]. He already states, that this is at least partially in contradiction with the findings of `Di Salvo et al.` [5]: They find a suppression of the CDW by possible intercalation and explain this by partial occupation of the conduction band. In the view of the Jahn-Teller effect, this occupation would even encourage distortion. However, as mentioned above, $TiSe_2$ is considered a semiconductor in the present work which contradicts the hypothesis of a Jahn-Teller effect as well as the experimental results found by water adsorption discussed in chapter 4 and 5 finding as well a suppression of the CDW by populating the conduction band. Though `Kidd`

et al. [33] state an "indirect Jahn-Teller effect" where the splitting takes place in the unoccupied states allowing a Jahn-Teller effect in a semiconductor, this extension still lacks elaboration and will not be developed further here.

Excitonic insulator

A first comprehensive discussion of a new, theoretically predicted insulating phase was given by Jérome et al. in 1967 [34] based on the work of Mott [35]. This phase can occur in a semimetal or a semiconductor possessing a small band overlap respectively gap. If the binding energy of an electron-hole pair, an **exciton**, is bigger than the gap and the Coulomb screening is weak due to a low carrier density, the system becomes unstable against the formation of excitons given sufficiently low temperatures. The formal description of this macroscopic ground state of condensed excitons is very similar to the BCS theory of superconductivity. But unlike a superconductor, this new ground state is an insulating one as the binding energy of the excitons has to be overcome to allow conduction. The modulation of the charge density here is a consequence of the non-zero momentum of the excitons connecting the valence band maximum at Γ with the conduction band minimum (see fig. 2.10).

Exciton condensate phase model

While Jérome et al. have developed their model for one dimension and isotropic band dispersion, Monney et al. [36] extended it to three dimensions and anisotropic dispersion. They call it **exciton condensate phase**, as they state a semimetallic normal phase finding the gap opening below the Fermi level and therefore not insulating. Ihle et al. found in a recent study [37] that the ground state might be considered of BCS-type for a semi-metallic high-temperature phase and a Bose-Einstein condensate for a semiconductor.

2.2.3 Application to $TiSe_2$

According to the experimental results presented in chapter 4, the exciton condensate phase model is considered the most promising here. Its application to $TiSe_2$ will be discussed following the *BCS-like approach* by Monney et al. [36].

Experimental evidence

The periodical lattice distortion in $TiSe_2$ has first been found with neutron diffraction studies by Di Salvo et al. [5] accompanied by a locally peaking electrical resistivity ρ (fig. 2.9). They define the critical temperature T_c as the minimum of the derivative $d\rho/dT$. The gradual formation of the superstructure and the anomaly in resistivity indicate a phase transition of second order. Their extended study of the influence of

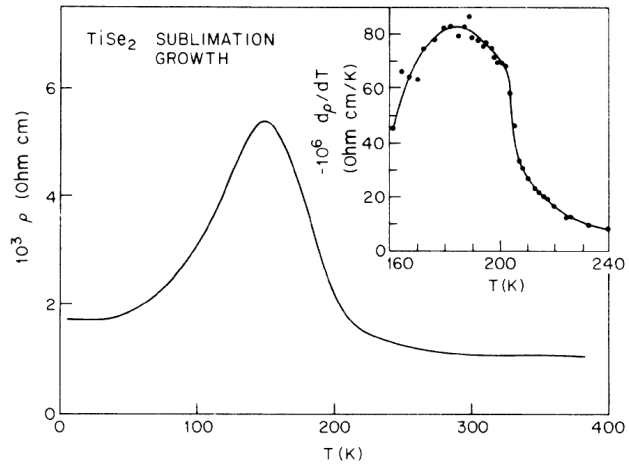

Figure 2.9: Resistivity in the plane $\perp$ to c in $TiSe_2$ grown by sublimation. The inset shows the derivative $-d\rho/dT$ [5].

different growth conditions showed a suppression of the transition by the intercalation of non-stoichiometric Ti. This in combination with their finding that the transition in TiS_xSe_{2-x} is suppressed for $x > 0.95$, `Di Salvo et al.` proposed an excitonic origin. While neutron diffraction allows to measure the atomic displacement vectors very accurately, later experiments e.g. by `Anderson et al.` [38] concentrated on the electronic structure by photoelectron spectroscopy studying the backfolded bands related to the evolution of the 2x2x2 superstructure in the CDW phase.

Electronic structure in the CDW phase

In the excitonic insulator phase, spanning vectors $\vec{w}$ connecting valence band maximum and conduction band are defined as they designate the momentum of the excitons forming between these points. For $TiSe_2$, the maximum of the valence band is located at Γ and the conduction band minimum at L. So there exist three spanning vectors $\vec{w}_i, i = 1, 2, 3$ connecting Γ with three symmetrically equivalent L points as shown in fig. 2.10. Thus an additional symmetry of the electronic structure in the excitonic condensate phase is introduced. From fig. 2.10 it can be deduced, that the original symmetry is maintained with the dimension bisected leading to the 2x2x2 superstructure. This superstructure has a purely electronic cause as a consequence of the centre of mass momentum of the excitons determined by the spanning vectors.

The shape of resized Brillouin zone is given in fig. 2.11 with its extension in all three directions cut in half. The A point of the original BZ becomes equivalent to the Γ^*

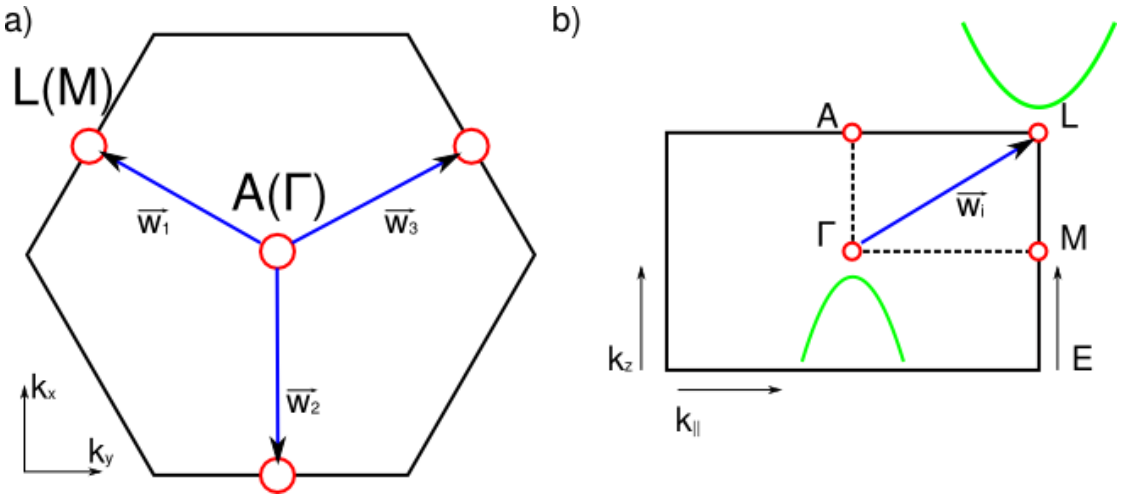

Figure 2.10: a) View of BZ with spanning vectors $\vec{w_i}$ along c direction b) View $\perp$ to c with bands in green.

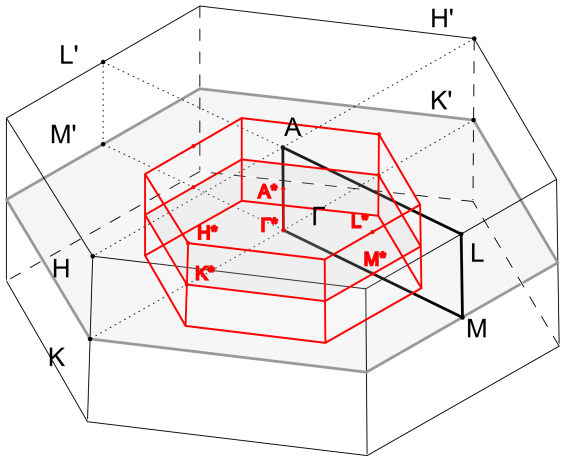

Figure 2.11: Brillouin zone of the normal phase (black) and resized BZ in the CDW phase (red).

point of the second resized BZ, as well as M and L become equivalent to Γ^* points. This superstructure can be directly seen in ARPES as e.g. the L point is now also the location of Γ^* and a new backfolded valence band maximum appears. Spectral weight is strongly transferred from the top of the valence band at Γ to the backfolded bands [39]. The atomic displacements of order $(0.03 - 0.09\,\text{Å})$ [5] in $1T-TiSe_2$ cannot explain this, other materials with stronger atomic displacements like $1T-TaS_2$ ($O(> 0.1\,\text{Å})$, [40]) exhibit

a much lower transfer. So the observation of this strong transfer favours the excitonic origin over a Jahn-Teller effect [29]. The appearance of the backfolded valence band is sketched in fig. 2.12 (not true to scale). Following the convention from [36], the topmost valence band is labeled v_1 and the visible conduction bands c_1, c_2 and c_3. The band c_3 will become important later, it is a backfolded conduction band from another L point [39]. The order parameter Δ quantifies the exciton formation and is seen as an indicator for the strength of the CDW phase. With increasing Δ, the valence bands are shifted towards higher binding energies. The binding energy of the excitons is probably in the order of the energy gap $E_g \approx 150\,\text{meV}$ [41] while `Pillo et al.` [42] estimate values around 15 meV. Thus the CDW phase is expected to have its main effect on the highest valence band and the lowest conduction bands, as their energy is so small.

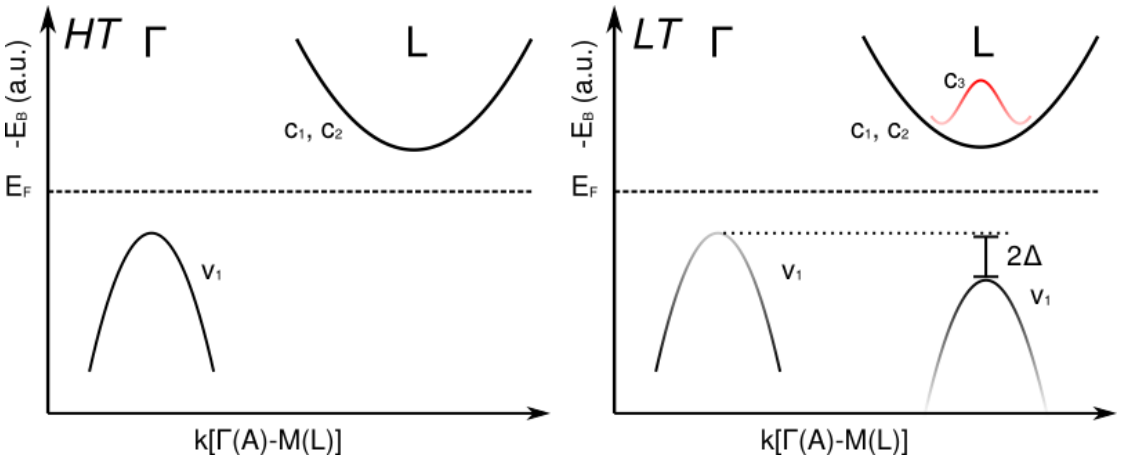

Figure 2.12: Scheme of the valence band v_1 and conduction bands c_1, c_2, c_3 with order parameter Δ at the symmetry points Γ and L for high temperature (HT) and low temperature(LT) adapted from [36]. Darker colour indicates higher spectral weight.

Excitonic fluctuations are already found around room temperature [29, 32, 38]. So the CDW phase is not fully destroyed well above T_c and bands are already shifted compared to the normal phase. This could be a reason for the long-standing discussion of the nature of the band gap in $TiSe_2$: Even at room-temperature measurements, the energy bands are already shifted due to fluctuations of the CDW phase.

2.2.4 Summary

$1T-TiSe_2$ with its very small indirect band gap is presently the only known candidate for an intrinsic excitonic insulator where no more influence than the low temperature is needed to drive the system into this new ground state. To probe the theory of an

excitonic insulator or condensate phase as driving force of the charge density wave, the evolution of the electronic structure in this phase has to be observed, which can be done with photoelectron spectroscopy. The influence of an altered population of the conduction bands as well as the size of the band gap could give hints whether the origin is electronic/excitonic or not: An increased population would hinder the formation of electron-hole pairs and a big gap size would prohibit their formation as their binding energy is relatively small. This was the motivation for the band gap engineering and the water adsorption experiments described in the following chapter 'Methods'. Resistivity measurements complete the study as the peculiarity of the anomaly in resistivity are regarded as a 'fingerprint' of the CDW phase characterising its strength.

3 Methods

In this chapter the methods used for sample preparation and analysis will be described. First, crystal growth and characterisation will be outlined. The introduction into the theory of photoelectron spectroscopy (PES) and its experimental application will follow. Furthermore, the technique of water adsorption to extend the analytical capabilities of PES will be described. Finally, the experiments to determine the transport properties will be sketched.

3.1 Crystal growth and characterisation

The crystals analysed here were grown by the technique of chemical vapour transport as introduced by Schäfer [43, 44]. By this method, outlined in section 3.1.1, high quality single crystals could be obtained. These were then analysed by energy-dispersive X-ray spectroscopy (EDX) to confirm their stoichiometry and by Laue diffraction to check their structural quality. These means of characterisation will be described in section 3.1.2.

3.1.1 Crystal growth by chemical vapour transport

Several techniques exist to grow single crystals as they usually cannot be found in nature. For large scale industrial purposes, e.g. silicon wafer production, a standard technique is the *Czochralski process*. However, this requires a smelter and for materials with high melting points like titanium (1660 K [45]) the technical realisation of high temperatures and the possible decomposition of the melt imposes difficulties. For the experiments carried out here, crystals of a size around 5x5 mm^2 were sufficient. Therefore, another technique not requiring melted materials could be used, the chemical vapour transport (CVT) technique.

In a chemical system containing solids and gaseous components, solid material can be transported via the gaseous phase if the equilibrium constant varies locally. This is realised for example by a temperature gradient $T_2 > T_1$ imposed on the system. At high enough temperatures $TiX_2$2 crystals can be grown by sublimation directly out of the constituent elements Ti and X (e.g. S, Se, Te). To reduce the necessary temperature, an additional substance like iodine forming a volatile compound with the educts can be introduced. In the zone with the starting materials, this will establish an equilibrium of the form

$$\mathrm{Ti}^s + \mathrm{I}_2^g \rightleftharpoons \mathrm{TiI}_2^g. \tag{3.1}$$

In the region of the lower temperature T_1, the diiodide dissociates to tetraiodide depositing the desired material. It is assumed, that X is in the gaseous phase, as the melting temperature for S, Se and Te is much lower than for Ti:

$$2\mathrm{TiI}_2^g + \mathrm{X}_2^g \rightleftharpoons \mathrm{TiI}_4^g + \mathrm{TiX}_2^s \tag{3.2}$$

The iodine is not expended throughout this process and therefore only a small amount of iodine is needed in a closed reaction volume. Depending on pressure and diameter of the reaction chamber, the transport between the zones is realised via diffusion or convection. For a detailed discussion of the technique in general, see e.g. [43, 44] and for its application on the TMDCs e.g. [46, 10].

The crystal growth conducted here used a clean evacuated quartz ampoule as closed container and iodine as transport gas. The educts Ti and X as well as the iodine were filled into the tube which was then evacuated to a pressure of $O(10^{-3}\,\mathrm{mbar})$ and sealed with a gas torch. To avoid evaporation of the iodine, the bottom of the ampoule holding the materials was kept in a bath of liquid nitrogen until the sealing was finished. After cleaning the outer part of the ampoule to avoid burn-in of dirt, it was placed into a four-zone furnace (see fig. 3.1). While the two outer zones serve as temperature buffer against ambient temperature, the inner two zones correspond to the temperature gradient $T_2 > T_1$. Under these conditions, diffusion transport is believed to dominate. Temperatures and growth times for the applied sets of growth conditions are given in table 3.1, all crystals except the last charge were grown under conditions A. Before the actual start of the growth, the growth area of the ampoule was cleaned by inverting the temperature gradient to remove potential contamination with residual educts. After the end of the growth time, the ampoules were slowly cooled down in the furnace.
Ternary crystals were obtained by replacing a fraction x of Se stoichiometrically by sulphur or tellurium.

Growth set	T_1 / C°	T_2 / C°	Time / min
A	740	780	18000
B	630	670	25000

Table 3.1: Growth conditions

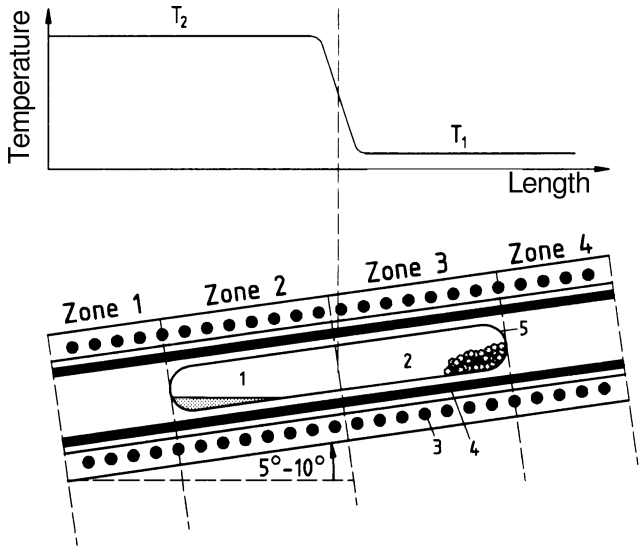

Figure 3.1: Furnace with temperature gradient $T_2 > T_1$. 1: Starting materials 2: Crystals 3: Ohmic heating 4: Ceramics tube 5: Quartz ampoule. Picture taken from [47].

3.1.2 Characterisation

After the growth was finished, the ampoules were cut open and the crystals were cleaned in alcohol. During a first optical characterisation under the microscope, the samples of interest were selected, sorting out crystals of obviously bad structural quality like screw dislocations and twins or too small size. To check the stoichiometry, the samples were characterised by EDX in the HU group "Physikalische Grundlagen der Photonik". The structural quality was checked by Laue diffraction in the physics department's facility. In the following these two characterisation techniques shall be discussed in more detail.

Energy Dispersive X-ray Spectroscopy

When electrons are removed from the inner shell, e.g. the K-shell, of an atom, the resulting electron vacancy is filled by an electron from an outer shell, e.g. the L shell. The energy freed by this electron falling deeper into the potential well of the nucleus leads to an emission of a high-energetic photon in the X-ray regime or the energy is transferred to another electron which then leaves the atom. The latter process is called the *Auger-Meitner effect*. As the energy levels are characteristic for an element, both effects can be used for spectroscopy determining the elements contained in a solid. The cross-sections depend on the atomic numbers Z: While the probability of the Auger-Meitner process is higher at lower Z and decreases with Z, the X-ray emission dominates for elements

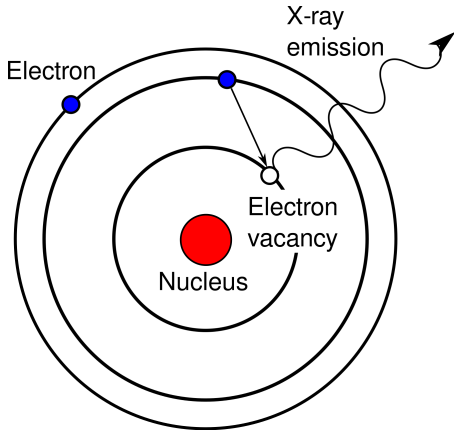

Figure 3.2: Principle of X-ray emission after excitation: An electron moves into the vacancy in a lower shell, the freed energy is emitted as X-ray.

with $Z > 30$. Therefore, X-ray spectroscopy is more accurate for heavy elements. Here, the samples were excited with an electron beam of 20-30 keV and the emitted photons were detected with a semiconductor detector yielding a characteristic Intensity($E_{h\nu}$) spectrum.

Laue diffraction

To determine the structural quality and orientation of a single crystal, Laue diffraction can be used. A continuous spectrum of X-ray light with energies up to 40 keV penetrates the sample. As the wavelength of the light is in the order of the atomic distances in the solid, it is diffracted if the wave vector $\vec{k_0}$ of the incoming light and the diffracted wave vector $\vec{k_1}$ fulfil the *Laue condition*

$$\vec{k_1} - \vec{k_0} = \vec{G} \tag{3.3}$$

where $\vec{G}$ is a reciprocal lattice vector. Due to the continuous spectrum this condition is easily fulfilled and many diffraction patterns can be seen without rotating the sample. In the backscattering setup used here, the sample can be analysed glued onto the sample screws of the PES system, a forward diffraction setup would require thin samples and a different mounting. While the determination of the exact crystal symmetry group by this method is possible e.g. with the help of well-known patterns [48], this was not the focus here. The hexagonal symmetry of the $1T-CdI_2$ easily allows a proper orientation and the number, intensity and sharpness of the diffraction patterns are a good indicator for the structural quality of the sample.

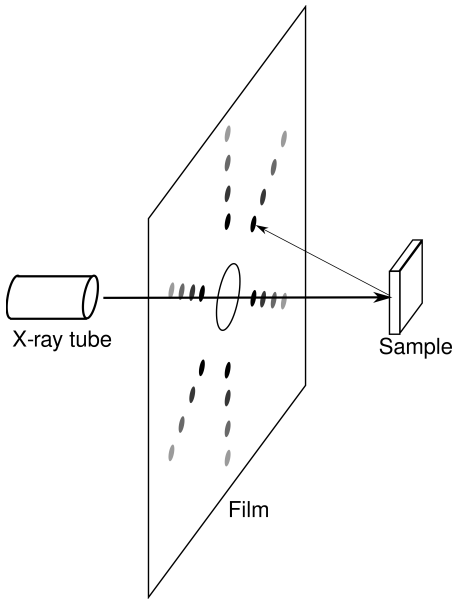

Figure 3.3: Principle of Laue diffraction in the backscattering setup: X-ray tube emits X-rays that are diffracted on the sample and detected as patterns on the film.

3.2 Photoelectron spectroscopy

One of the most important experimental techniques for the determination of the electronic structure of a solid is the photoelectron spectroscopy (PES) based on the photoelectric effect discovered by Hertz in 1887 [49]. Electrons are removed from a sample with incident light and are then detected dependent on their kinetic energy. If also the emission angles ϕ and θ (see fig. 3.4) are resolved, it is called **angular resolved photoelectron spectroscopy** (ARPES). In case of energies in the UV (10-100 eV) range it is referred to as ARUPS. The latter was used to measure the change in the valence band structures of the studied crystals in course of their phase transition. An important aspect of PES is the fact, that it is only sensitive to the surface.

3.2.1 Theory

The basic theoretical background for this method was provided by Einstein's explanation of the photoelectric effect [50] in 1905. Incident light can remove electrons from a sample if its energy is higher than a material-dependent threshold, the work function Φ. The maximum kinetic energy $E_{kin,max}$ of the photoelectrons then is linearly increasing with shorter wavelengths of the incident light. The photocurrent is proportional to

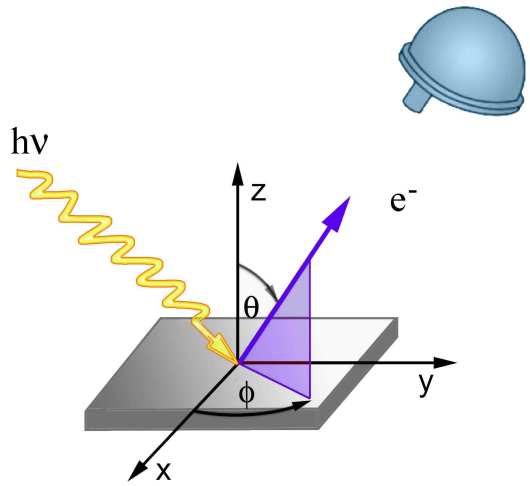

Figure 3.4: Principle of ARPES. Incident light $h\nu$ removes electrons from a sample that are collected by a spectrometer resolving energy and emission angles Φ and Θ. Picture taken from [51].

the intensity of the light and sets in immediately. Einstein explained this stating light quantums, the photons, interacting with the electrons in the solid. One photon gives its energy $h\nu$ to one electron which can leave the solid with a maximum kinetic energy

$$E_{kin,max} = h\nu - \Phi \tag{3.4}$$

if it is not scattered inelastically, see fig. 3.5. It has to be added, that this is actually only true for metals, where the Fermi level E_F is observable. If the energy is high enough, the photons can also remove electrons from energy levels below E_F with a binding energy E_B:

$$E_{kin} = h\nu - \Phi - E_B. \tag{3.5}$$

By typical convention, E_B will be given positive numbers here, if the energy level is below the Fermi level towards the occupied states. The energy levels are sketched in fig. 3.5.

To get a complete view of the band structure in the solid, the distribution of the electrons with respect to their binding energy and their momentum in the solid, the initial state $\vec{k_i}$ has to be known. So the outgoing electrons removed by the incident photons are analysed with respect to their kinetic energy and their momentum $\vec{p}$, with

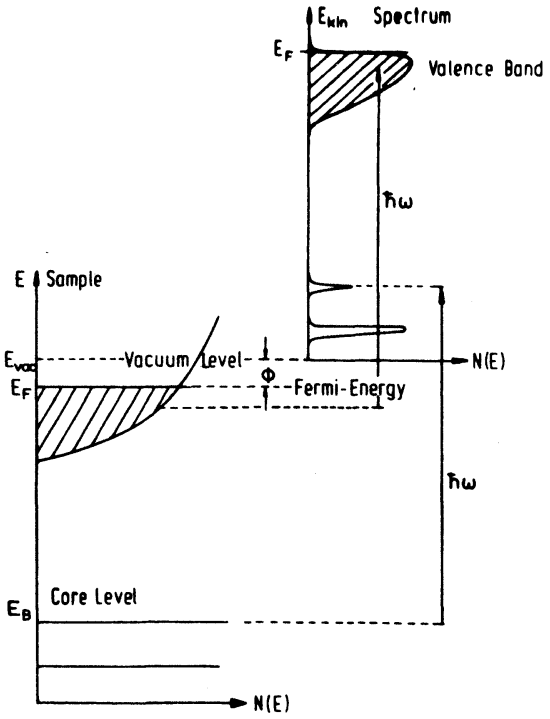

Figure 3.5: Energy levels in PES [52]: Vacuum level E_{vac}, Fermi level E_F, work function Φ, binding energy E_B.

m being the mass of the electron:

$$p = \sqrt{2mE_{kin}} \tag{3.6}$$

To obtain the direction of $\vec{p}$, the angles ϕ and θ of their emission have to be resolved. Given that, it is possible to gain information of the initial states of the electrons using different theoretical models.

3.2.2 Three- and One-Step Model

The most common description of the photoemission process is the so called three-step model, which will be discussed here. First, the electron is excited within the solid into a final state, then it travels to the surface and from there escapes into the vacuum. The probabilities for these processes are multiplied. The division into these steps is an artificial simplification, but yet, this model has proven useful as first approximation.

Another simplification used here is the sudden approximation: The interaction between the excited electron and the remaining N-1 electron system is considered to take place so fast that it can be neglected.

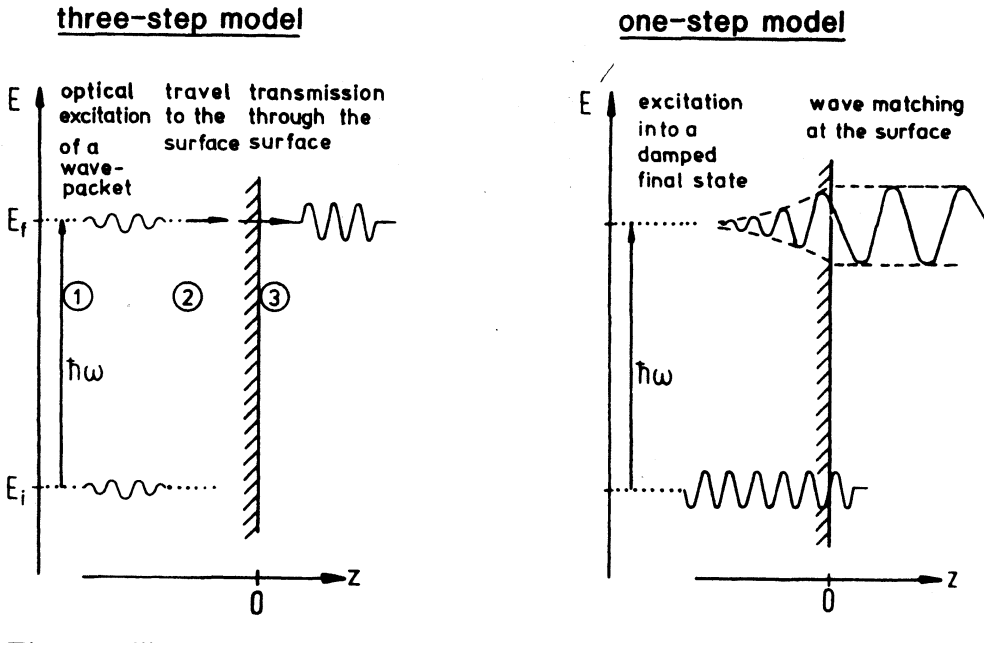

Figure 3.6: Comparison Three- with One-step model [52].

Step One: Optical excitation

For the energies $h\nu < 100\,\mathrm{eV}$ considered here, the momentum of the photon is much smaller than the typical size of a Brillouin zone and therefore disregarded, so we can assume the optical excitation to be a direct transition between the initial state $\vec{k_i}$ and the final state $\vec{k_f}$. In the reduced zone scheme, this is a vertical $\vec{k_f} = \vec{k_i}$ transition, while the extended zone scheme one has $\vec{k_f} - \vec{k_i} = \vec{G}$ with the reciprocal lattice vector $\vec{G}$.

Applying first order time-dependent pertubation theory one calculates the transition probability ω between the initial state with the N-electron wave function $|\Psi_i^N\rangle$ and the final state $|\Psi_f^N\rangle$ with their energies E_f and E_i by Fermi's Golden rule:

$$\omega = \frac{2\pi}{\hbar} \left|\langle \Psi_f^N | H_{int} | \Psi_i^N \rangle\right|^2 \delta\left(E_f - E_i - h\nu\right) \tag{3.7}$$

The interaction operator H_{int} describes the applied pertubation by the electric field given by the vector potential $\vec{A}$ and the electron momentum $\vec{p}$ neglecting non-linear processes like two photon processes:

$$H_{int} = \frac{e}{mc}\vec{A}\cdot\vec{p} \tag{3.8}$$

Step Two: Transport to the surface

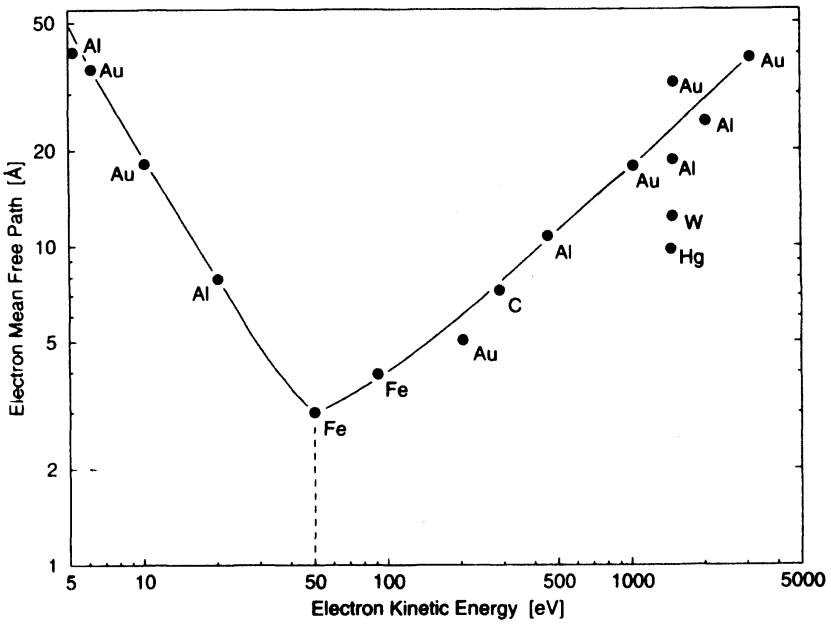

Figure 3.7: Universal curve for the electron inelastic mean free path [52].

The excited electrons are scattered by collisions with phonons and electrons on their way from the bulk to the surface. As electron-phonon scattering is mainly relevant at very low energies, the dominant effect determining the mean free path λ of the electrons is electron-electron interaction [52]. Of the N_0 electrons, that were excited at depth z from the surface, only N escape under the angle *theta* (to the surface normal) without loosing energy due to inelastic scattering.

$$N = N_0 \exp\left(\frac{-z}{\lambda\cos\theta}\right) \tag{3.9}$$

The resulting mean free path (see fig. 3.7) is roughly the same for all materials. For this curve, the electrons are described by the approximation of the free electron gas[1]. Then, the loss function is only determined by the mean electron-electron distance

[1]This approximation is actually only a good one for $E_{kin} \gg E_B$ [52].

being (another approximation) the same for all materials. So the probability that the excited electron will travel to the surface maintaining the information of its initial state is proportional to λ while the inelastic scattering gives rise to a background of secondaries which is usually ignored or subtracted using a "Shirley-type" background [53].

Step Three: Escape into the vacuum

In the free electron final state model, the final Bloch states in the bulk are described by nearly-free electron parabola with zero at the bottom of the valence band E_0. The final states in the vacuum are described by a free electron parabola with zero at the vacuum level E_V. Though this assumption is more accurate for alkali metals, it is also used for atoms with more complicated electron shells with the disadvantage of another approximation.

Due to the potential step on the surface, electrons are diffracted to larger angles outside the crystal (see fig. 3.8). In order to escape the solid, the component $\vec{k}_{f\perp,int}$ of the electrons' final state which is normal to the surface, has to be higher than the surface potential barrier $E_0 + \Phi = V_0$. This barrier is the so-called "inner potential". The other electrons that have a $\vec{k}_{f\perp,int}$ too small, are reflected back into the solid:

$$\frac{\hbar^2 k_{f\perp,int}^2}{2m} \stackrel{!}{\geq} V_0 \tag{3.10}$$

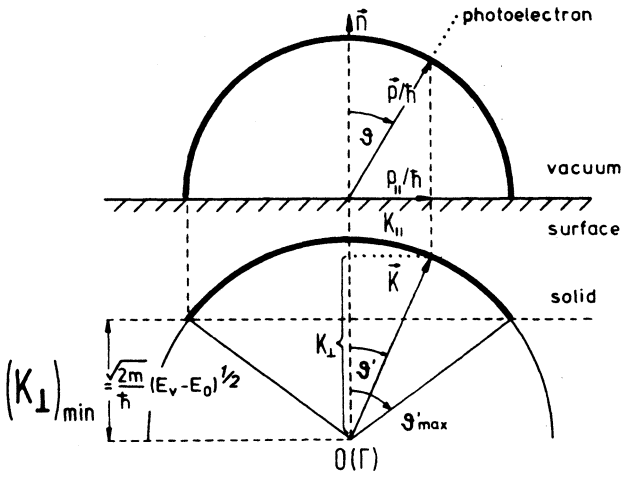

Figure 3.8: Escape condition [52]. $\vec{K}$ and $\vec{p}$ are the wave vector within respectively outside the solid, $\vec{n}$ the surface normal, θ the emission angle, θ' the angle of the propagation within the solid and θ'_{max} the maximum angle that allows an escape into the vacuum.

The component parallel to the surface $\vec{k}_{f\parallel,int}$ is conserved (see fig. 3.9) and with the perpendicular component of the electron momentum outside the crystal, $\vec{p_\perp}$, the kinetic energy is determined:

$$\vec{k}_{f\parallel,int} = \frac{\vec{p}_\parallel}{\hbar} = \frac{1}{\hbar}\sqrt{2mE_{kin}}\sin(\theta) \tag{3.11}$$

$$E_{kin} = \frac{\hbar^2}{2m}\left(\vec{k}^2_{f\parallel,int} + \frac{{p_\perp}^2}{\hbar}\right) \tag{3.12}$$

With the parameters $\vec{p}$ and E_{kin} directly observable in ARPES, the component $\vec{k}_{f\perp,int}$ remains undetermined within this model. If the inner potential V_0 is determined e.g. by LEED, one can obtain the missing component:

$$\vec{k}_{f\perp,int} = \frac{1}{\hbar}\sqrt{2m\left(E_{kin}\cos^2\theta + |V_0|\right)} \tag{3.13}$$

In low-dimensional systems like $TiSe_2$, the dispersion along the c axis is quite small so that the uncertainty in the determination of $\vec{k}_{f\perp,int}$ is often neglected as the band structure is mainly determined by $\vec{k}_{f\parallel,int}$. The dispersion of the valence band maximum at Γ to A is for example only 40 meV [4]. However, the structure is expecially for binding energies $E_B > 1\,\mathrm{eV}$ not completely flat, as can bee seen e.g. in $k_\perp$ maps from `Thürmer` [12].

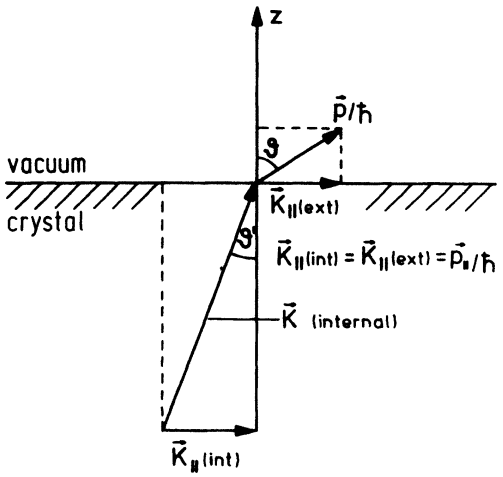

Figure 3.9: Momentum relations [52]. $\vec{K}$ is the electron momentum inside the crystal, $\vec{p}$ outside, θ is the angle of the electron inside and θ' outside the crystal.

Step one until eq. 3.8 is common for most models. The difference is the description of the final state in the matrix element $\left|\langle\Psi_f^N|H_{int}|\Psi_i^N\rangle\right|$. While in the three-step model,

it is the final Bloch eigenstate inside the crystal, the more accurate final state in a one-step model is the "reversed LEED" state, see fig. 3.6 and e.g. [52] or [54] for further discussion.

Photocurrent

The resulting current of photoelectrons $I(\vec{k},\omega)$ escaping due to excitation by photons with $E = \hbar\omega$ is in this model proportional to the single-particle spectral function $A(\vec{k},\omega)$ and the one-electron dipole matrix element $\left|M^{\vec{k}}_{f,i}\right|$. The single particle spectral function is the probability by which the electron can be excited from its ground state and is proportional to the imaginary part of the Green's function $G(\vec{k},E)$.

$$I(\vec{k},\omega) \propto \left|M^{\vec{k}}_{f,i}\right|^2 A(\vec{k},\omega) \tag{3.14}$$

3.2.3 Experimental aspects

The light source used here was synchrotron radiation, other light sources used for PES are X-ray tubes, gas discharge lamps or lasers. The structure of valence bands is typically investigated with energies in the UV regime (5-100 eV), e.g. the He I line (21.2 eV) due to better energy and momentum resolution. The information depth is limited by the mean free path for elastically scattered electrons, which is only a few Å for the used energy range, see fig. 3.7. Therefore, PES is very surface sensitive and requires UHV conditions with samples cleaved or annealed in situ.

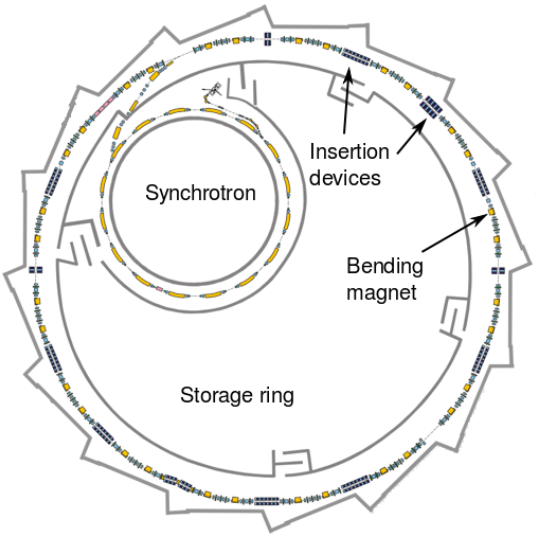

Figure 3.10: Map of the Beamlines at BESSY, adapted from [55].

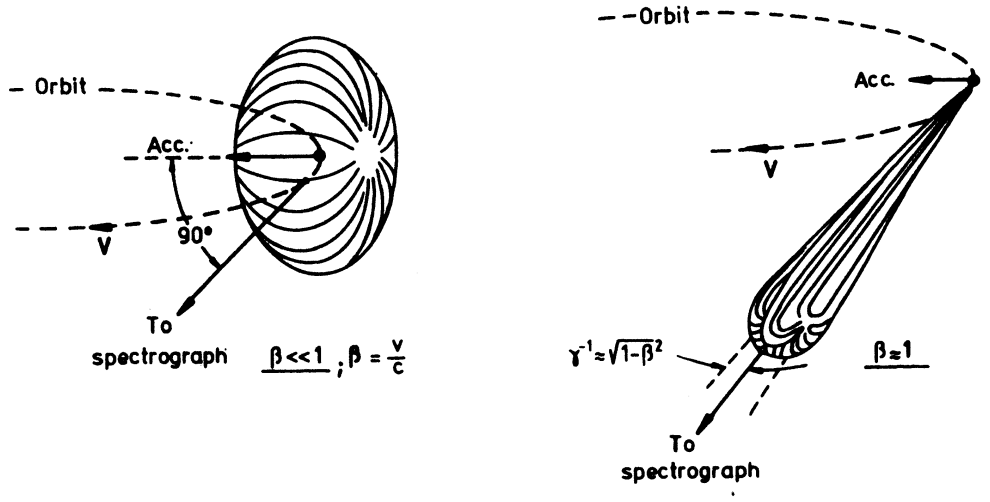

Figure 3.11: Radiation characteristic of relativistic electrons [52]. v: velocity of the electrons.

Synchrotron radiation

When relativistic charges are accelerated radially by a magnetic field, they emit tangential radiation called synchrotron radiation. In a synchrotron particles like electrons are accelerated by a high-frequency electric field and held on an approximately circular path by magnets. With increasing energy ($v/c \approx 1$) the particles become more relativistic and their emission of radiation peaks in forward direction, see fig. 3.11.

To keep their path static, the electric and magnetic fields are synchronized to this energy gain. At the third generation synchrotron light source BESSY II, the electrons produced by an electron gun are first accelerated in a microtron to 50 MeV, and then further accelerated in a synchrotron to 1.7 GeV before they are injected into the storage ring which has a circumference of 240 m, see fig. 3.10.

There, the radiation is produced at several arrangements of magnetic fields: Bending magnets are needed to keep the electrons on track while insertion devices like undulators and wigglers are arrays of magnets specially designed to create high intensity radiation of a wide energy range ranging up to hard X-rays. The light produced is used at approx. 50 beamlines.

Due to the high-frequency electric field in the accelerating cavities, the electrons form packets with an overall current of max. 300 mA. Scattering on residual gas in the storage ring as well as small errors in the electron optics lead to a gradual loss of intensity over time. After 8 hours, the current has fallen to approx. 150 mA and new electrons are injected into the ring.

Hemispherical analyser

The standard detectors today are hemispherical electron analysers (fig. 3.12). In the angular mode, which was used here, photo-excited electrons from a sample are collected in an electrostatic lens system and their kinetic energy is changed to a pass energy E_p. Then they pass through an entrance slit into the spherical deflection analyser, which is basically a capacitor kept at a certain potential. The direction of the angular and energetic dispersion are perpendicular. After passing an exit slit, the electrons impact on a 'micro-channel-plate' (MCP), a 2D array of electron multipliers. The multiplied and accelerated electrons then illuminate a phosphor plate, the image is detected by a CCD camera. This gives a distribution of the electrons over different emission angles proportional to $\vec{k}_{\|}$ at fixed kinetic energy. The image of the band structure is then created by selecting consecutive kinetic energies in the lens system. For a more detailed discussion, see e.g. [12].

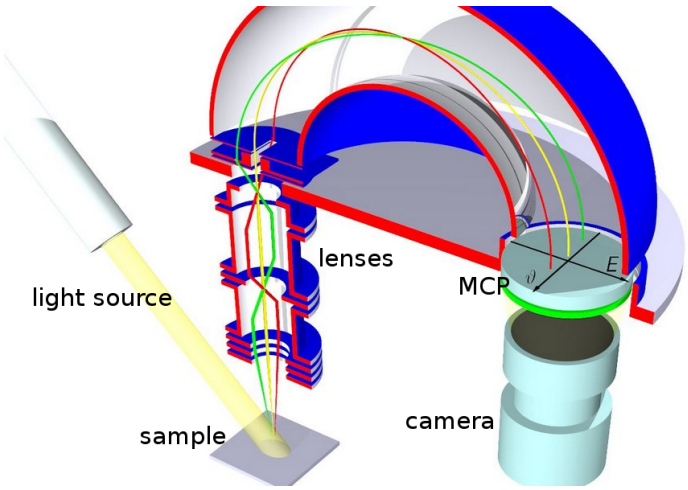

Figure 3.12: Principle of the electron spectrometer adapted from [56]. Different colours of the electron orbits indicate different emission angles/values for $\vec{k}_{\|}$.

Resolution

The effective resolution of ARPES in energy space, ΔE, can be split into two parts: Experimental causes and a signal broadening due to thermal fluctuations determined by the Fermi function. The latter has a width $4k_BT$ which is $\simeq 100\,\mathrm{meV}$ at room temperature $T = 300\,\mathrm{K}$. Assuming that the count rate is high and one can neglect statistical effects, the experimental signal broadening is determined by instrumental errors. The width of the light source's energy distribution is very small for gas discharge lamps but for synchrotron radiation, errors in beamline optics and slit sizes increase it

considerably: For the setup described later, the overall resolution is 25 meV, with approx. 20 meV coming from the light beamline. The resolution of a hemispherical detector is determined by the used pass energy $E_p = O(5\,\mathrm{eV})$, the radius of the electron orbit R, the slit size of the entrance slit s and the acceptance angle α:

$$\Delta_E = E_P \left(\frac{s}{2R} + \alpha^2 \right) \tag{3.15}$$

α is defined as the maximum angle to the slit normal under which an electron can enter the entrance slit and still passes the exit slit. Setting the kinetic energy of the electrons to the relatively low pass energy has the advantage, that the energy resolution is enhanced without changing the energy distribution of the electrons. However, a low pass energy also reduces intensity. The angular resolution is determined by the accuracy of the sample positioning, the electron optics of the detector and the resolution of the CCD camera.

Location in the BZ

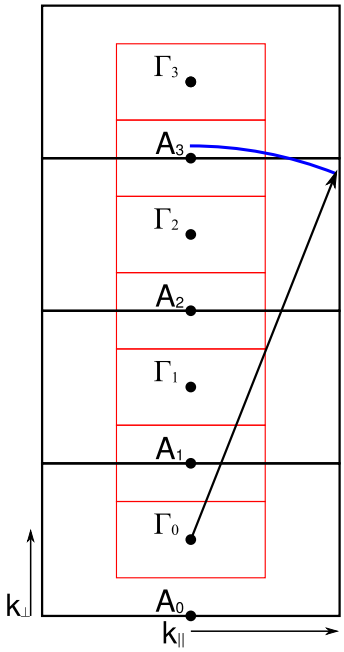

Figure 3.13: Scanning location in the BZ of $TiSe_2$ for the applied excitation energy $h\nu$. Original BZ in black, resized BZ (2x2x2 superstructure) in red, measurement position defined by a circle (blue) with radius $h\nu = 22\,\mathrm{eV}$. Adapted from [42].

Typically, the measurements are carried out at a fixed energy and $\vec{k}_{\parallel}$ is varied by tilting the sample. The disadvantage is, that $\vec{k}_{\perp}$ is also changed by the tilt. Fig. 3.13 shows the situation for $TiSe_2$ and $h\nu = 22\,\text{eV}$, the vector $\vec{k}$ is constant and defines a circle around Γ_0 indicated in blue. Increasing the measured $\vec{k}_{\parallel}$ by tilting the sample reduces $\vec{k}_{\perp}$ as the length of the vector is dependent on $h\nu$ which is kept constant. For normal emission around the valence band maximum $E_{kin} \approx 17.1\,\text{eV}$, an inner potential of $V_0 = 10.5\,\text{eV}$ [12] and ΓA=0.526 Å^{-1}, $\vec{k}_{\perp}$ is close to A: With (3.13) one gets $k_{\perp}(17.1\,\text{eV})/\Gamma\text{A} \approx 5.1$.

3.2.4 Instrumental set-up at BEST

Beamline

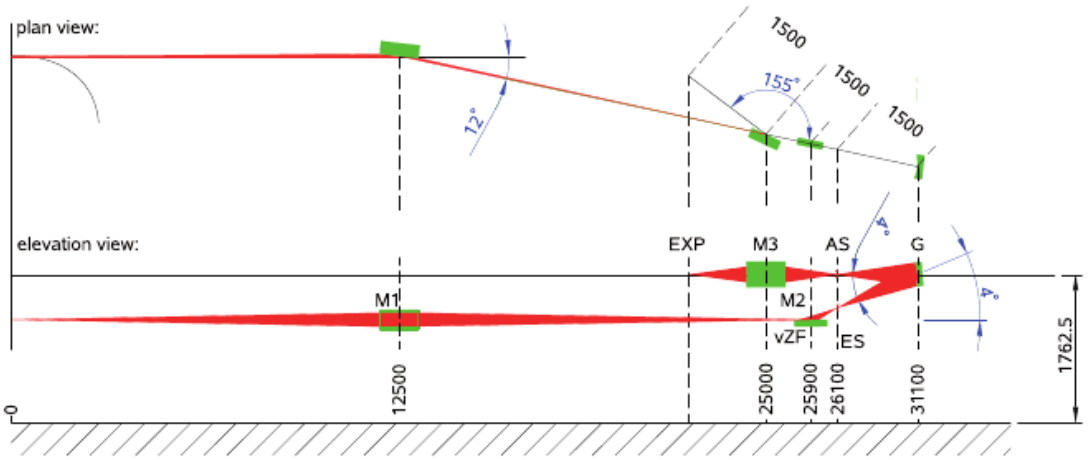

Figure 3.14: Sketch of BEST [57]. M_1, M_2 and M_3 are mirrors, G is the grating, ES and AS are entry and exit slit, EXP is the experimental chamber.

The light for the beamline for education and scientific training (BEST), light is produced at a dipole bending magnet. From its characteristic continuous spectrum of available energies, the desired energy is selected with a 5 m normal incidence monochromator (NIM) after it has passed two mirrors focusing and changing the direction of the beam (fig. 3.14). Passing the third mirror M3 it enters the docked experimental station (fig. 3.16).

The NIM consists of a curved grating with 1200 lines per mm and a curvature radius of 5006 mm in a moveable vacuum tank and two slits 5 m away from the grating with an opening angle of 4°. The wavelength of the diffracted light is selected by rotating the grating which is mounted according to the Off-Rowland principle which means that

the grating is moved on the angle bisector and that the slits have the same distance to the Rowland-circle. The Rowland circle is defined as a circle with half the radius of the curved grating touching it. A point lying on the circle is again focused onto it. With the current set-up, energies ranging from 15 to 40 eV can be used with reasonable intensity (fig. 3.15)[2].

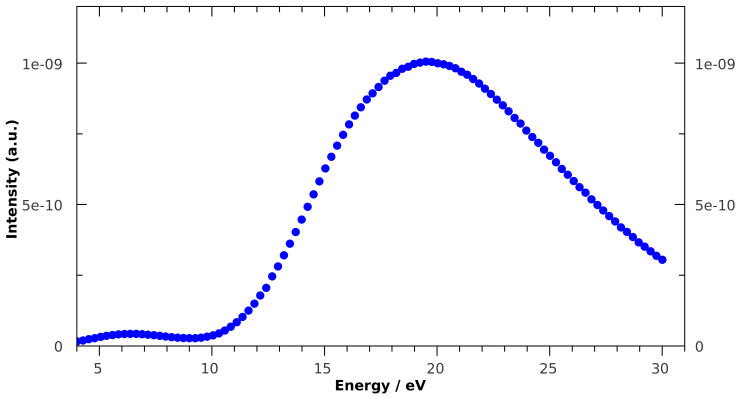

Figure 3.15: Intensity distribution of the monochromator.

Experimental chamber

In the experimental chamber the sample is mounted on a cryogenic manipulator cooled with liquid He allowing a variation of the temperature between 20 K and room temperature. The temperature is controlled via a PID controller connected to an ohmic heating which allows a temperature stability <1 K. The sample position can be varied via 5 axes, the translation directions x, y and z as well as two rotation directions. The R_1 axis is vertical, while the R_3 axis is horizontal. The R_3 direction is the same in which the angular distribution in the detector is resolved. The whole experimental station is depicted in fig. 3.16, for a detailed description of the system see e.g. [12, 57, 58]. The pressure in the experimental chamber is $\simeq 7 \cdot 10^{-11}$ mbar with the manipulator at low temperature and $\simeq 2 \cdot 10^{-10}$ mbar at room temperature. The effective angular resolution of the setup is of $O(0.1°)$.

Sample holders and transfer system

The samples are glued onto aluminium sample screws with a two-component epoxide silver adhesive. Together with a counter-screw for convenient orientation, the sample

[2] With the installation of a new grating by the end of 2010, the energy range will be extended down to 5 eV.

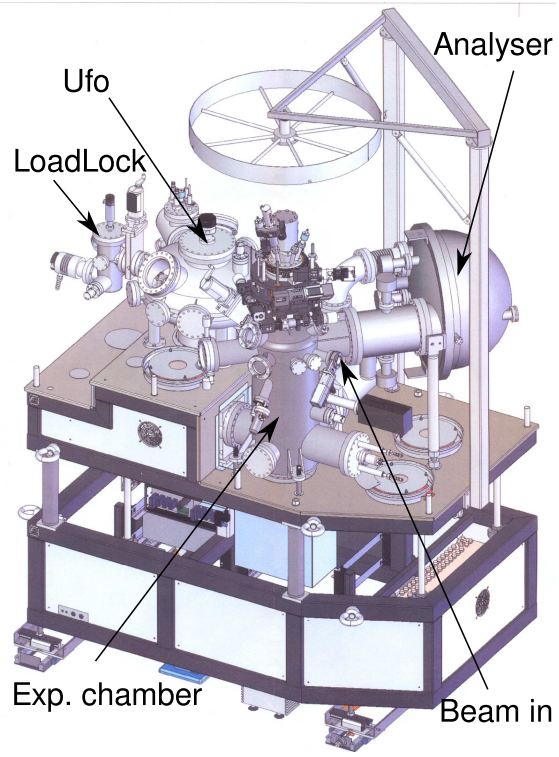

Figure 3.16: The experimental station at BEST adapted from [59].

screws are mounted onto a copper sample holder. This sample holder has the option for a second clamping-screw that can be screwed into the cryogenic manipulator for better cooling and mechanical contact. Up to six holders can be mounted in the Load Lock, where the samples enter the experimental station. From there, they can be distributed over the transfer chamber (Ufo), where the pressure is $\simeq 7{\cdot}10^{-10}$ mbar, to the preparation chamber or the experimental chamber.

Sample orientation

To obtain a defined scanning orientation during the APRES experiment, the samples have to be properly orientated according to their crystal structure. Crystals of good quality show a well-defined macroscopic hexagonal shape (see fig. 4.1). By Laue diffraction measurements, it was confirmed that this corresponds very well to the microscopic structure. So the hexagonal BZ has the same shape and orientation as the macroscopic crystal. However, one has to distinguish between the symmetry points L and L' as the PES signal strength is much lower at L'. While the manipulator range of the R_3 direction is mechanically limited in one direction, this was at the utilised photon energy

h$\nu = 22\,$eV just enough to reach both points rotating in positive or negative direction to compare the signal strengths. If the sample was tilted too much on the sample holder, it had to be removed from the chamber and rotated 60°.

3.3 H_2O adsorption

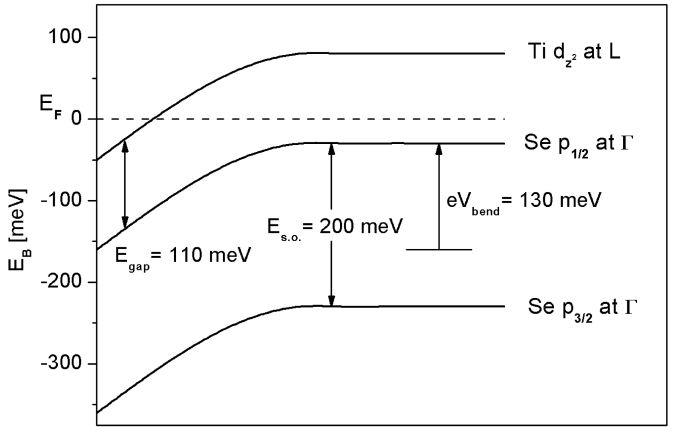

Figure 3.17: Band bending (Schottky-like) induced by H_2O [4]. c indicates the direction normal to the surface, $E_{s.o.}$ is the spin orbit splitting, eV_{bend} is the bending in energy, E_F is the Fermi-level, Ti, Se are the energies of the corresponding bands.

To answer the question whether a material is a semiconductor, the existence of an energy gap E_g between the maximum of the occupied valence band and the minimum of the unoccupied conduction band has to be probed: If this gap exists ($E_g > 0$), the material is a semiconductor or insulator $E_g \gg 0$. With ARPES only occupied energy bands are observable, as the incident light can only remove electrons from there. Only under certain conditions thermally occupied bands are accessible up to $5k_BT$ above E_F [42]. This inconvenience can be partly overcome by the use of inverse photoelectron spectroscopy, but this technique suffers from a lower energy resolution and a small cross section of the inverse photoemission process [52]. Investigating the electronic nature of $TiSe_2$ with ARPES, `Rasch et al.` [4, 60] have overcome this problem occupying the conduction band by means of water adsorption inspired by adsorption experiments of `Karschnick et al.` [61]. As the TMDCs have no dangling bonds on the surface, water molecules are ideally physisorbed only by the van der Waals force creating a Schottky-like contact. In a simple model described e.g. by `Thürmer` [12], the dipole moment of the H_2O molecules reduces the work function as a function of the adsorbed amount of water and changes the charge carrier density at the surface. This leads to a **Schottky-**

like contact sketched in fig. 3.17 bending the conduction band below E_F. With an increasing amount of water, a saturation can be found, which is probably due to one monolayer of H_2O molecules sticking on the surface [12]. Due to the surface sensitivity of PES, only those shifted bands are monitored. The adsorbates can be removed e.g. by heating and the original spectrum is recovered [61].

3.3.1 Experimental realisation

To deposit water on a clean sample surface, H_2O vapour was introduced via a valve into the Load Lock chamber at the beamline. The vapour was produced by breaking an ampoule of distilled water in fore-vacuum connected via a valve to the Load Lock chamber of the experimental station. For the quantification of the water exposition, the unit Langmuir (L) from surface science is used:

$$1\,\mathrm{L} = 1.33\,\mathrm{mbar} \cdot 1\,\mu\mathrm{s} \tag{3.16}$$

The actual deposition of H_2O molecules also depends on the sticking coefficient S, as not every molecule hitting the surface sticks to it. With $S = 1$, 1 L corresponds to one monolayer. `Thürmer` [12] finds a sticking coefficient of $\simeq 2 \cdot 10^{-4}$ for $TiSe_2$, in good accordance with [61]. For a more detailed description of the experimental set-up, see [12].

3.4 Electrical resistivity

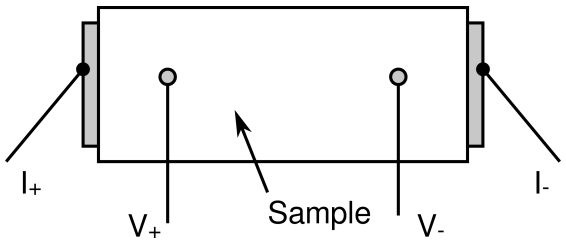

Figure 3.18: Sample contacts for resistivity measurements. $I_{+/-}$ are the contacts for the current, $V_{+/-}$ the contacts for the potential.

The transport properties of the samples were determined with the commercial system Quantum Design PPMS 6000. This system allows to measure resistivity, AC susceptibility and Hall-resistivity in a temperature range of 2 - 370 K. For a detailed description of the system, see e.g. [62, 63].

3.4.1 Realisation

For the measurement of the resistivity, the four-point method (see fig. 3.18) was used: Two large contacts (labelled I in fig. 3.18) on the side faces were used to create a homogeneous current through the sample of which the dimensions were carefully determined. Two point-shaped contacts (labelled V) served to measure the potential drop caused by the resistivity. As now current flows through these contacts, the contact resistivity is irrelevant here. The contacts were made of gold wire and silver lacquer, which was baked at 100 °C for 1 h for some experiments.

4 Results and discussion

In this chapter, the execution of the experiments will be described and their results will be presented. In the first section, the grown crystals and the results of their stoichiometric and structural analysis will be given. The second section is devoted to resistivity experiments which are generally regarded as an indicator for the strength of the phase transition. Photoelectron spectroscopy measurements under different conditions and for different samples will be presented in the third section allowing to examine their electronic structure. The discussion in the theoretical context will conclude this chapter.

4.1 Crystal growth

The crystal growth is of essential importance for the subsequent experiments. ARPES experiments require high quality mono-crystals and the CDW phase transition is very sensitive to the growth conditions.

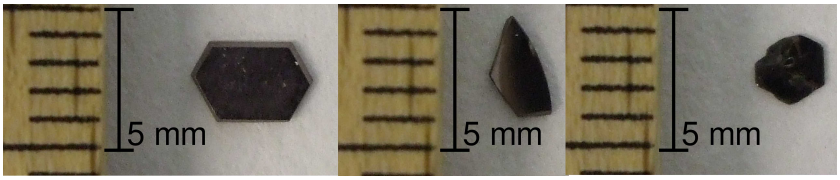

Figure 4.1: Single crystals. Left: $TiSe_2$. Middle: $TiTe_{0.04}Se_{1.96}$. Right: $TiS_{0.13}Se_{1.87}$.

Several charges of $TiSe_2$ were grown at the same conditions using a temperature gradient from $T_1 = 740\,°C$ to $T_2 = 780\,°C$, the growth time t was set to 18000 min. As transport gas iodine was used and the educts were weighed in stoichiometrically. The ampoules were sealed at a pressure $p < 10^{-2}$ mbar. For one charge, an electrical power outage in the laboratory lead to an abortion of the growth process after less than 4500 min. The resulting crystals were much smaller, approximately half the width in the direction perpendicular to c and one third in c direction. However, the quality was not affected as confirmed by EDX and Laue diffraction. The last charge of $TiSe_2$ was grown at lower temperatures $T_1 = 630\,°C$ and $T_2 = 670\,°C$ in order to check the influence of the growth temperature on the phase transition. Due to the lower temperature, the growth time was chosen to be 25000 min. After the growth process was finished and the ampoules had slowly cooled down, they were cut open. The part with the educts (right

part of fig. 4.2), that was at in the zone with T_2, still contained some of the educts as well as crystals of different sizes in one big array. Very much iodine was still left in this part and the stoichiometry was expected to vary. Thus this part of the growth was removed. The part of the ampoules intended for the actual growth contained bigger crystals of different sizes (left part of fig. 4.2) that were carefully taken off the quartz and then cleaned in ethanol to remove residual iodine. Only crystals that showed at least partly hexagonal shape (see fig. 4.1) and that were not grown together with other crystals were selected for further analysis. The macroscopic hexagonal shape simplifies crystal orientation and indicates a good quality in terms of stoichiometry and crystal structure. In the grown-together crystals, so-called *twins*, the orientation of the structure can vary locally which can lead to incertitudes in orientation.

Figure 4.2: Results of crystal growth ($t < 72\,\mathrm{h}$). Left in plastic cointainer: Crystals from zone T_1. Right: Mixture of educts and crystals from zone T_2 with iodine.

For the **ternary compounds** $TiTe_xSe_{2-x}$ and TiS_xSe_{2-x} the educts were weighed in stoichiometrically and were also grown with a temperature gradient from $T_1 = 740\,^\circ\mathrm{C}$ to $T_2 = 780\,^\circ\mathrm{C}$ with the same time $t = 18000\,\mathrm{min}$. In the first charge of TiS_xSe_{2-x} 10 % of the Se atoms were substituted by S, which was expected to result in $x = 0.2$. The second charge was prepared with $x = 0.4$ to get $TiS_{0.4}Se_{1.6}$. For $TiTe_xSe_{2-x}$, 10 % of Se were substituted by Te to obtain $TiTe_{0.2}Se_{1.8}$.

The **EDX measurements** were conducted standardless at a beam energy of 20 keV by Dr. Peter Schäfer. Standardless means that no well-defined reference spectrum was used, so the signal was normalized to Ti_y, $y := 1$. Four specimen as representatives of one growth were given to the analysis. This was justified by the finding that the variation of stoichiometry of different preselected crystals was much smaller than the errors imposed by the measurement. The results averaged over a selection of samples from one charge

Material	Charge #	Ti	Se	S	Te
$TiSe_2$	1	1.00 ± 0.08	2.10 ± 0.35	-	-
$TiSe_2$	2	1.00 ± 0.08	2.30 ± 0.37	-	-
$TiSe_2$	3	1.00 ± 0.08	2.00 ± 0.22	-	-
$TiS_xSe_{2-x}, x = 0.2$	1	1.00 ± 0.08	1.95 ± 0.32	0.13 ± 0.02	-
$TiS_xSe_{2-x}, x = 0.4$	1	1.00 ± 0.08	1.66 ± 0.27	0.33 ± 0.03	-
$TiS_xTe_{2-x}, x = 0.2$	1	1.00 ± 0.08	2.00 ± 0.33	-	0.05 ± 0.01

Table 4.1: EDX results normalized to Ti:= 1.00, x is the fraction of the educts.

are given in table 4.1. It can be seen, that only a fraction of the intended sulphur and tellurium were incorporated into the crystals. As the absolute errors for x are smaller than the errors for the selenium content, the ternary compounds will be named after the content of sulphur and tellurium respectively, the Se content will be adapted which can be justified by the big errors for Se in the order of 0.3. Consequently, the denotation for the ternary compounds will be $TiS_{0.13}Se_{1.87}$, $TiS_{0.33}Se_{1.67}$ and $TiTe_{0.05}Se_{1.95}$ in the following.

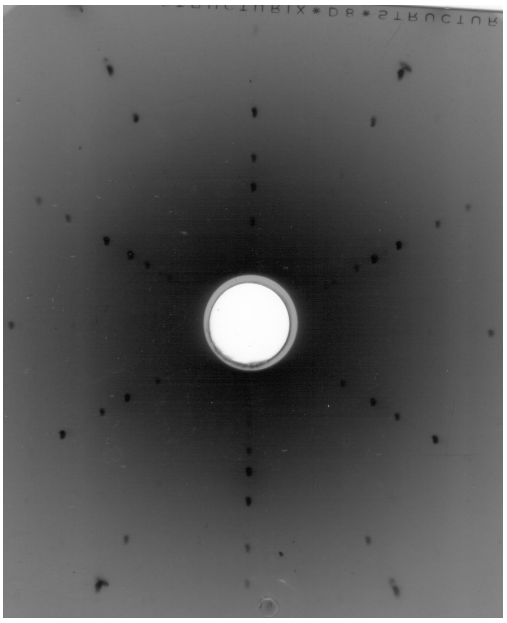

Figure 4.3: Laue diffraction image of $TiTe_{0.05}Se_{1.96}$. Black spots represent diffraction patterns.

For **Laue diffraction**, specimen of the charges that were already mounted on the

sample screws used in the PES setup have been analysed. Diffraction patterns of several orders arranged in a sixfold symmetry can be seen very clearly which indicates a good structural sample quality. Consequently, only one example is given in fig. 4.3.

4.2 Resistivity

The electrical resistivity $\rho(T)$ is regarded as an indicator for the sample quality with respect to the CDW phase transition [5]. `Di Salvo` defines the critical temperature T_c as the local minimum of the derivative $d\rho/dT$ finding $T_c = 202\,\mathrm{K}$ and states the ratio $\rho_{max}/\rho(300\,\mathrm{K})$ of the maximum resistivity ρ_{max} to the value at 300 K to be a good indicator for the sample quality [5]. Hence the electrical resistivity of different crystals $TiSe_2$ and the ternary compounds was analysed in the Quantum Design PPMS 6000 system between 2 K and 300 K. The applied frequency of the 20 mA alternating current was 30 Hz and the temperature alteration rate was set to 1 K/min. The contacts were made with gold wires glued to the sample with silver contact lacquer. Some contacts were baked for 1 h at 100 °C, but it was found that the resistivity curve was more stable and had a much more pronounced hump without baking.

4.2.1 $TiSe_2$

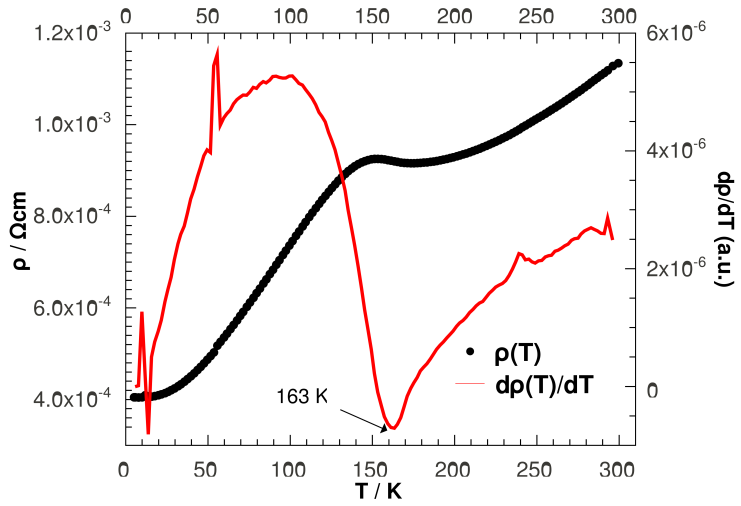

Figure 4.4: Resistivity ρ (black) and derivative $d\rho/dT$ (red) of $TiSe_2$ grown at $T_g = 740\,^\circ\mathrm{C}$.

For $TiSe_2$ grown at $T_1 = T_g = 740\,^\circ\mathrm{C}$ the maximum in resistivity (fig. 4.4) is not very pronounced and the minimum in the derivative of the resistivity can be found at 163 K while the value for the resistivity ratio is $\rho_{max}/\rho(300\,\mathrm{K}) = 0.82$. The results for $T_g = 630\,^\circ\mathrm{C}$ (fig. 4.5) show a more pronounced maximum with $\rho_{max}/\rho(300\,\mathrm{K}) = 1.47$ and the peak in the derivative shifts to a significantly higher temperature 191 K compared to the samples grown at higher temperature. It can also be seen, that the resistivity

shows no hysteresis, the curve in fig. 4.5 contains the data points from 300 K to 2 K and back.
Measurements of the Hall-coefficient by `Brabetz` [63] indicate that $TiSe_2$ is an n-type semiconductor which could be an indicator for doping with excess Ti [5].

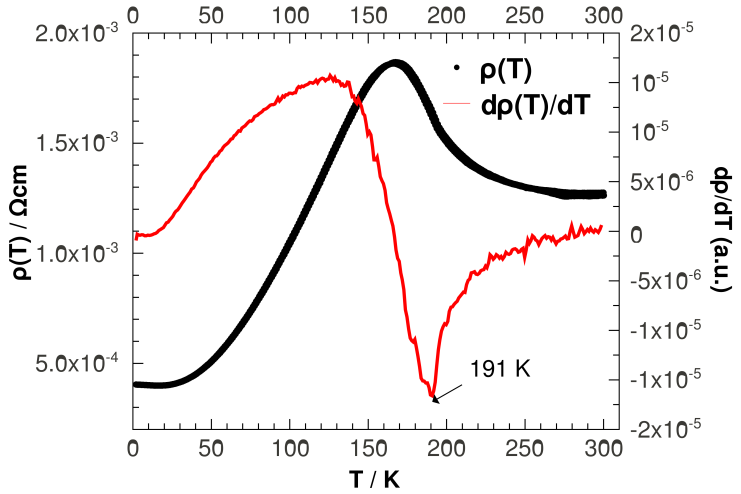

Figure 4.5: Resistivity ρ (black) and derivative $d\rho/dT$ (red) of $TiSe_2$ grown at $T_g = 630\,^{\circ}C$.

4.2.2 Ternary compounds

The ternary compounds evidence an even less pronounced peak in resistivity. The results for TiS_xSe_{2-x} with $x = 0.13$ and $x = 0.33$ are shown in fig. 4.6(a). With an increasing content of sulphur the peak in resistivity shifts to lower temperatures and becomes less pronounced. As a local maximum of $\rho(T)$ cannot be found any more, only the minima of $d\rho/dT$ are given. They are located at $T_c = 133\,K$ for $x = 0.13$ and $T_c = 94\,K$ for $x = 0.33$. For $TiTe_{0.05}Se_{1.95}$ (fig. 4.6b) not even a minimum in $d\rho/dT$ can be found, the trend is monotonous.

4.2.3 Comparison with literature

`Di Salvo et al.` [5] find a very pronounced resistivity peak for sublimation growth (see fig. 2.9) as well as for iodine vapour transport. While the resistivity for the sublimation curve shows a more semiconductor-like behaviour with an increasing resistivity for a decreasing temperature, their samples show a different slope for CVT, the resistivity decreases with temperature which is also found for all samples here. `Di Salvo et al.` conclude, that this is due to residual iodine in the samples in the order of 0.3 at. %, which

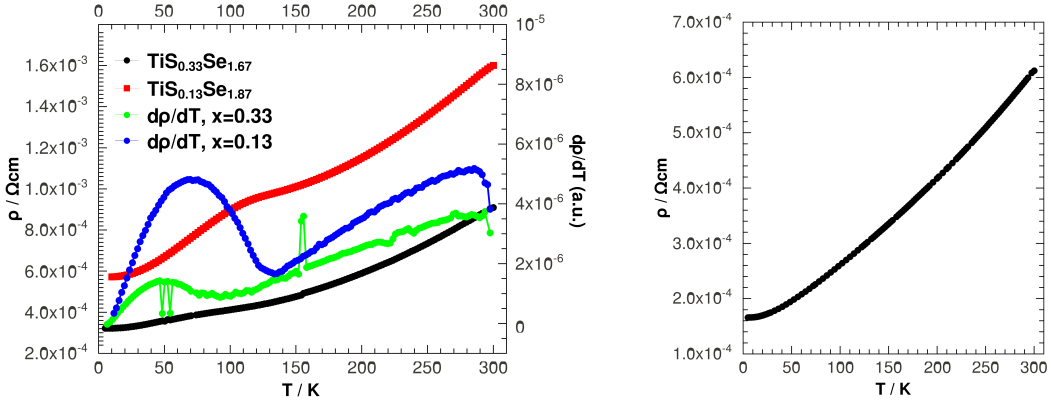

(a) (b)

Figure 4.6: a) Resistivity ρ (black & red) and derivative $d\rho/dT$ (green & blue) of TiS_xSe_{2-x} with $x = 0.13$ and $x = 0.33$. b) Resistivity of $TiTe_xSe_{2-x}$ with $x = 0.05$.

could also be true for the samples presented above. However, such a low iodine content could not be resolved by the EDX measurements performed in this study. They also find a decreasingly pronounced maximum with growing sulphur content as it is found here as well, though also for the ternary samples, their maxima are more pronounced. The weaker maximum found here could be a feature of the contacting method. Nevertheless, the presented resistivity curves are comparable among each other, as they were contacted the same way.

4.3 ARPES

The results of the photoelectron spectroscopy measurements are presented in the following. First, the evolution of the CDW with temperature in $TiSe_2$ is given. Then, the ternary compounds are presented as well as an evolution of $TiSe_2$ spectra with an increasing amount of water. Finally, spectra for a sample grown at lower temperature will be shown.

4.3.1 Preparation

The clean samples were glued to sample screws with a two-component epoxide silver adhesive baking it for 1 h at 100 °C. A clamping screw can be inserted into the sample holder (fig. 4.7) which allows screwing it tightly to the manipulator in the experimental chamber allowing a better cooling contact. After this procedure the samples were orientated according to the desired measurement direction. Where an aluminium lever was

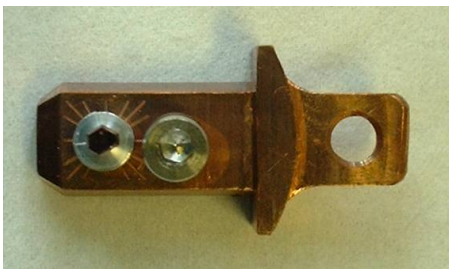

Figure 4.7: Cu sample holder with sample and clamping srew.

used for cleaving, the L-shaped lever was fixed to the sample using the same procedure as fixing the sample to the sample screw.

4.3.2 Execution

After the samples were installed in the Load Lock of the experimental system of BEST, it took several hours until a pressure in the order of 10^{-8} mbar was achieved. Most samples were cleaved with adhesive tape that was fixed to the sample and the carousel in the Load Lock. They were cleaved by transferring the samples into the Ufo chamber where the pressure was in the low 10^{-9} or high 10^{-10} mbar. Other samples were cleaved using an L-shaped cleaving lever fixed to the sample either in the Ufo or directly in the main chamber. The disadvantage of this method is the loss of a bigger portion of the sample while the advantage is a better pressure for the cleaving resulting in a cleaner sample surface. This difference became negligible when the repaired turbo molecular pump (TMP) for the Load Lock replaced the temporarily installed pumping station.
During the measurements with cooling the PID controller was used to select the temperature for the sample. When the temperature was changed the PID had to adapt to the new settings resulting in a temporarily oscillating temperature. To assure a good temperature stability of at least $< 2\,\mathrm{K}$ and to make sure that also the sample surface had adapted to the temperature, the system was allowed to settle down for approx. 30 min before the start of the next measurement. The lowest temperature achieved varied between 20 K and 30 K due to an internal heat bridge in the manipulator that appeared randomly and was only fixed near the end of the measurement time.
Slit sizes for the beamline were set in the order of $50\,\mu$m and a curved detector slit of 0.5 mm width was selected. The **Fermi level** E_F was determined either by evaporating gold onto the sample and then measuring a reference spectrum around the Fermi cut-off or by using a special sample holder with freshly evaporated gold. An upper limit for the resolution ΔE could be gained by this procedure as well, which was found to be $\Delta E \approx 25\,\mathrm{meV}$.

H_2O adsorption

For the H_2O adsorption experiments, the cleaved sample was introduced into the Load Lock again. The pumping power of the TMP was reduced by partly closing a valve between the chamber and the pump. H_2O vapour was then introduced into the chamber over a needle valve up to a pressure of $O(5 \cdot 10^{-5})$ mbar for a time of $O(100)$ s. The desired amount of H_2O was calculated with eq. 3.16.
Before the actual H_2O adsorption, a reference spectrum of the clean sample at low temperature was recorded. As the sticking coefficient is higher for cold surfaces, the sample temperature had to be set to room temperature again allowing the sample enough time to heat up which turned out to be especially important for thick samples.

4.3.3 $TiSe_2$

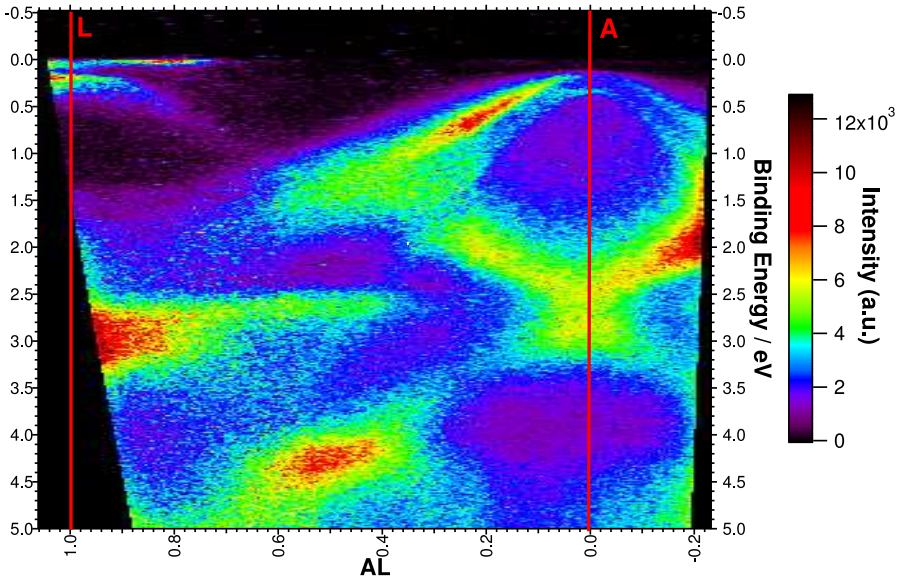

Figure 4.8: Overview spectrum of $TiSe_2$ at 28 K in AL direction with backfolded band at symmetry point L and maximum of valence band at A.

Figure 4.8 shows an overview spectrum in AL direction taken at 28 K well in the CDW phase. The red lines show the location of the symmetry points A(Γ) and L(M). With increasing binding energy the spectrum shows a smaller width in $k_\parallel$ due to the dependence of $k_\parallel$ on the kinetic energy (eq. 3.11). The maximum of the valence band can be identified at A, the Ti $3d$ emission is located near E_F at L as well as the backfolded bands, that can be traced up to a binding energy of approx. 1 eV. As the phase transition only affects bands near E_F, only the valence band maximum around A and

the backfolded bands around L will be considered in the following. Furthermore, the consideration will be restricted to the L point as the backfolded bands are visible at much higher intensities compared to L' (see fig. 4.9), while the form is widely the same. This difference can be explained with the symmetry argument in chapter 2.

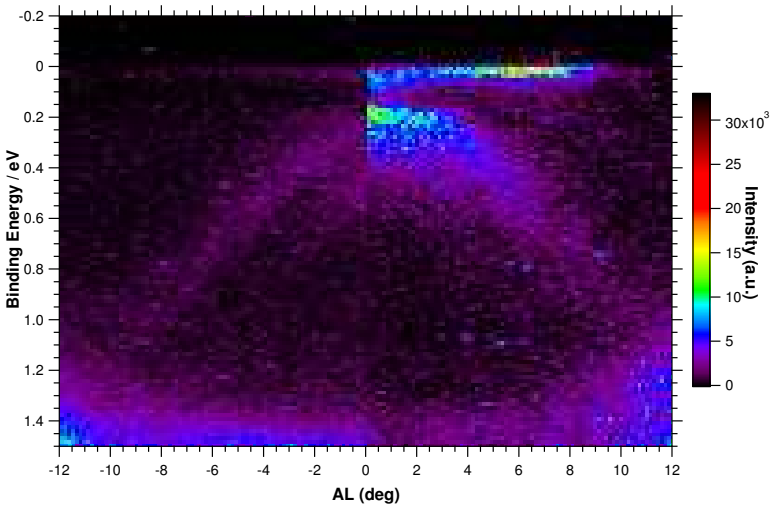

Figure 4.9: Spectrum around L'(left) and L (right) at 28 K.

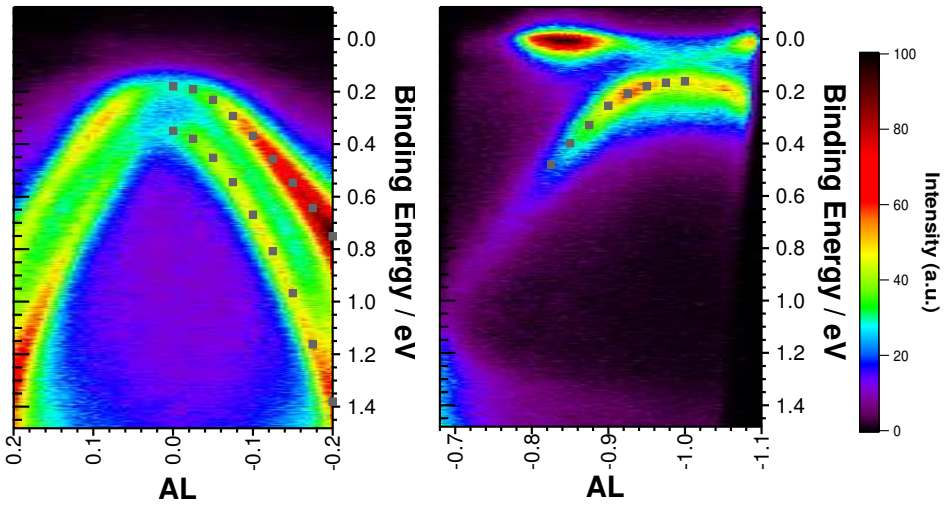

Figure 4.10: Spectra at A (left) and L (right), T=21 K. Dots indicate the maxima of the bands. The x axis indicates the relative distance between A and L.

A more detailed comparison of A and L at low temperature $T = 21\,\mathrm{K}$ is given in fig. 4.10. Grey dots indicate the maxima of the bands. These were obtained by extracting an energy distribution curve (EDC) from the respective spectrum with a width of 1% the length of the distance AL. The EDC was then fitted with a multi-peak fit using a *Voigt*[1] profile as peak shape. The extracted results are given in fig. 4.11 together with a parabolic fit to obtain the effective masses m_e^* for the bands using the dispersion relation:

$$E(k) = \frac{\hbar}{2m_e^*}k^2 \tag{4.1}$$

$$\frac{1}{m_e^*} = \frac{1}{\hbar^2}\frac{d^2E(k)}{dk^2} \tag{4.2}$$

The results for the bands A_1, A_2 and L_1 and their energy offsets E_0 at the symmetry points A and L are given in table 4.2. It can be seen that the effective mass of the backfolded band differs from the masses of the two uppermost valence bands and that it is shifted to slightly lower binding energies towards the Ti $3d$ emission by about 50 meV compared to A_2.

Band	m_e^*/m_e	E_0 / meV
A_1	0.28 ± 0.01	205 ± 12
A_2	0.16 ± 0.01	385 ± 13
L_1	0.38 ± 0.01	157 ± 5

Table 4.2: Effective masses m_e^* and energy offset E_0 of the bands A_1, A_2 at A and L_1 L at $T = 21\,\mathrm{K}$.

[1] Convolution of Gauss (experimental resolution) and Lorentzian (line shape).

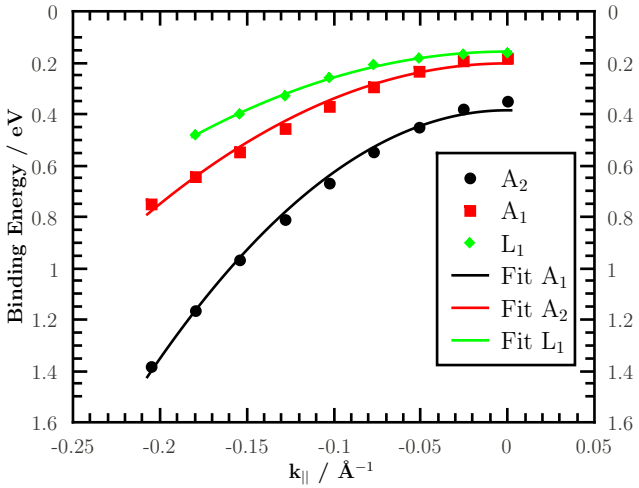

Figure 4.11: Parabolic fit of the bands A_1, A_2 at A and L_1 at L.

Temperature evolution The evolution of the backfolded bands with increasing temperature will now be considered. Fig. 4.12 shows the spectra at L for low temperature $T = 24\,\mathrm{K}$ and moderately high temperature $T = 140\,\mathrm{K}$. At higher temperatures the intensity of the backfolded bands decreases and it shifts towards E_F. For low temperatures the upper, Ti $3d$ related emission, clearly shows two very strong contributions 0.2 AL away from L that decrease quickly towards L. According to `Kidd et al.` [33] this is due to an interaction between valence band and the conduction band: In a strong CDW phase, the backfolded valence bands are not parabolic any more, but 'flat topped' and the minimum of the conduction band is not at L any more. See also fig. 2.12, with the band c_3 shifted downwards. For 140 K their relative intensity decreases and the intensity at L increases. This emission just below E_F now looks more like a band with relatively high effective mass. Comparing this with the model in fig. 2.12 it looks like the two strong emissions come from the conduction band labeled c_3 and the band with the flat dispersion is the conduction band c_1. Consequently, the conduction band c_3 experiences a stronger shift at lower temperatures towards the backfolded bands.

To get a more detailed insight into the evolution of the bands, EDCs with a width of 1 % AL were extracted at L. Again, a multi-peak fit was applied. The background was approximated as linear and the peak shapes as Voigt. For the uppermost peaks, the Voigt profile was additionally convoluted with the Fermi-Dirac cut-off. Peak positions and shapes could be reproducibly obtained by this procedure. A detailed example is given in fig. 4.13. At 24 K four contributions can be clearly identified, which is in good accordance e.g. with [39]. The contributions A and B near E_F are related to the Ti $3d$ orbital and the peaks C and D to the spin-orbit split Se $4p_{3/2}$ and Se $4p_{1/2}$ band. At this

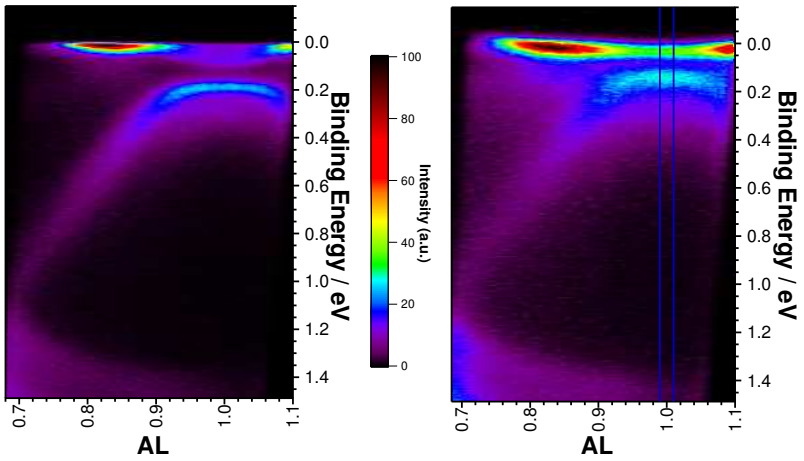

Figure 4.12: Comparison of the region around L at 24 K (left) and 140 K (right). The two blue lines in the right image define the integration area for one EDC.

temperature, the intensity of A and B is about half the intensity of the Se $4p_{3/2}$ peak C. The positions of the peaks are given in table 4.3. The gap between the Ti $3d$ emission A and the Se $4p_{3/2}$ emission C is 160 meV. At 140 K only one peak can be identified below E_F at the same position as A but with higher intensity, C shifts around 40 meV towards E_F while D remains at the same position. The gap between A and C is now only 110 meV.

T / K	A / meV	B / meV	C / meV	D / meV
24	29 ± 1	78 ± 2	188 ± 1	282 ± 3
140	28 ± 1	-	144 ± 1	275 ± 14

Table 4.3: Locations of the peaks A,B,C and D for $TiSe_2$ at 24 and 140 K, extracted with a multi-peak fit.

Intermediate steps in the evolution with temperature up to 170 K of another sample are given in a waterfall plot in fig. 4.14. Unfortunately, the signal of the CDW phase was not as strong for this sample as for other samples and the CDW seems to disappear earlier, the signal at 70 K is very similar to the signal at 140 K in fig. 4.13. Still, the main features of the temperature evolution can be seen clearly: With increasing temperature the Ti $3d$ peak becomes sharper, more intense and moves towards E_F. This corresponds well with the expectations, as the normal phase of $TiSe_2$ is a semiconductor with the conduction band above E_F. The relative intensity of the Se $4p$ emission diminishes

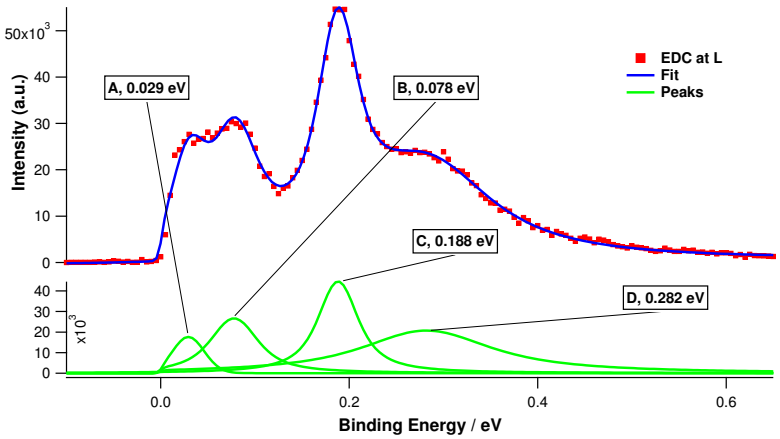

(a)

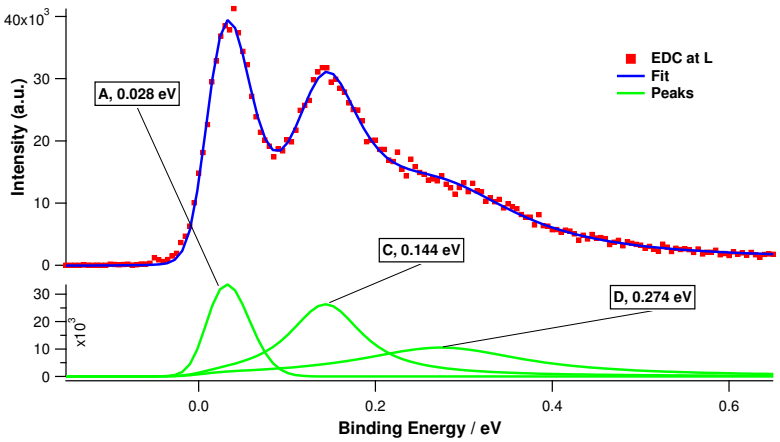

(b)

Figure 4.13: EDCs of $TiSe_2$ at L for $T = 24\,\mathrm{K}$ (a) and $140\,\mathrm{K}$ (b). Experimental data (red) is given together with the fit (blue) and its different contributions (green).

and the upper, $4p_{3/2}$, emission shifts to lower binding energies. A direct comparison of the intensities turns out to be difficult as the manipulator moves in z direction with increasing temperature, approx. 1 mm between low temperature and room temperature. This changes the signal strength, the sample has to be readjusted and a direct comparison would become very inaccurate. A temperature evolution of a better signal can be seen in figures 4.17 and 4.18. Albeit the sample is a ternary $TiS_{0.13}Se_{1.87}$ one, the evolution is qualitatively the same.

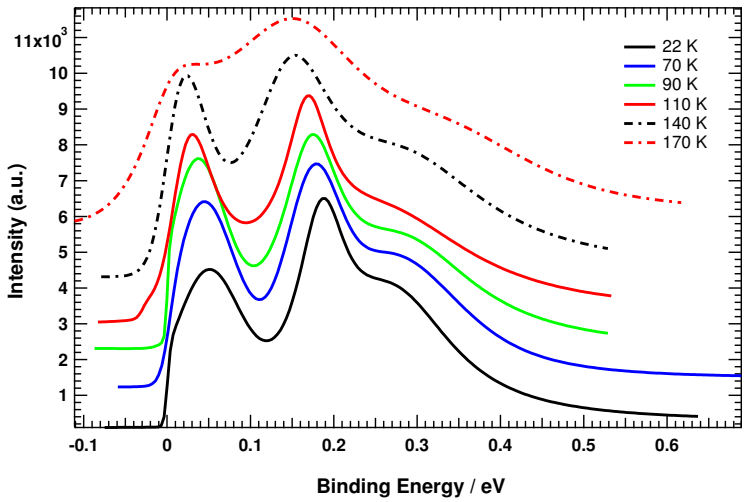

Figure 4.14: Waterfall plot of the intermediate steps of the temperature evolution for $TiSe_2$. The curves represent the corresponding fits, normalized to peak C.

Thus it can be seen that an increasing temperature destroys the charge density wave phase. In the view of the excitonic model this is due to the excitons provided with an increasing energy by thermal fluctuations and finally breaking up.

4.3.4 Ternary compounds

The ternary compounds TiS_xSe_{2-x} with $x = 0.13, 0.33$ and $TiTe_xSe_{2-x}$ with $x = 0.05$ are considered here. If one assumes a linear change in the size of the band gaps with the stoichiometric factor x (see fig. 2.5), the gaps should be 170 meV and 200 meV for the sulphur samples with $x = 0.13, 0.33$ and 103 meV for $TiTe_{0.05}Se_{1.95}$.

The ternary compounds were analysed in the same way as the $TiSe_2$ samples above, their temperature evolution was studied and especially the spectra at low temperatures were analysed in more detail. Figure 4.15 shows the comparison of two temperatures $T = 31$ K and $T = 140$ K for the ternary compound $TiS_{0.13}Se_{1.87}$. The spectra look very similar to the results for $TiSe_2$, which still holds after a more detailed analysis of the EDC at L given in fig. 4.16. Again, four contributions can be identified with the Ti $3d$ peaks A and B exhibiting about half the intensity of the Se $4p_{3/2}$ peak C.

The evolution of the EDC at L with increasing temperature is given in fig. 4.17. It shows the fits at the different temperatures normalized to peak C. Until a temperature of 110 K, the contributions A and B can still be distinguished, but for higher temperatures they merge into one broad peak. While the position of D does not change very much, C shifts to lower binding energies with increasing T. The relative intensity of the Ti $3d$

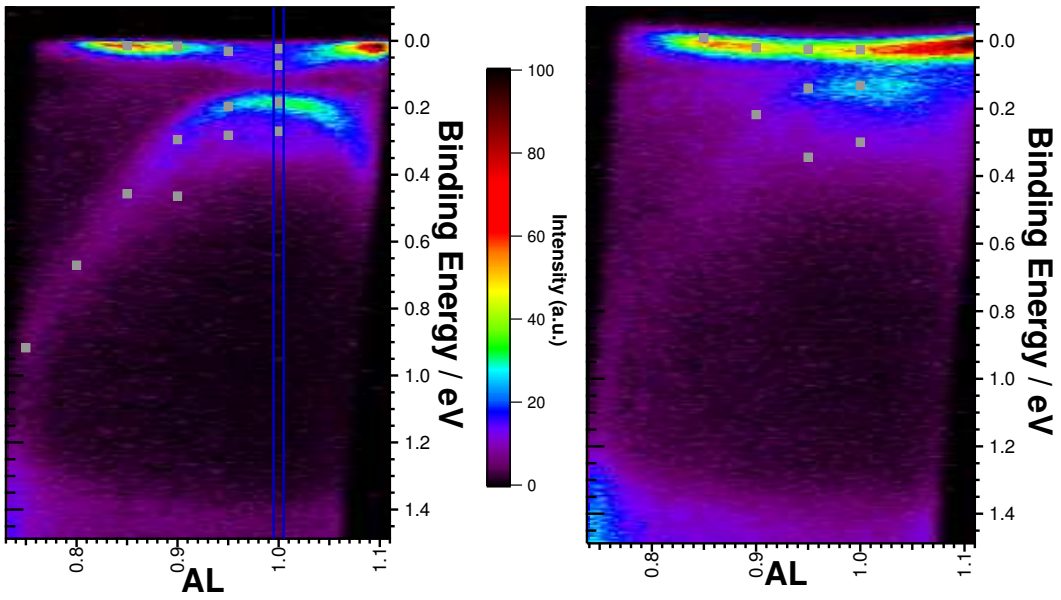

Figure 4.15: Comparison of the region around L at 31 K (left) and 140 K (right) for $TiS_{0.13}Se_{1.87}$. Dots indicate maxima obtained by fits, the two blue lines in the left image define the integration area for one EDC.

emission is smaller than C, but becomes notably higher for temperatures above 110 K while it starts to decrease at 213 K. The positions of the different peaks together with the fit errors are given in table 4.4.

T / K	A / meV	B / meV	C / meV	D / meV
31	26 ± 3	79 ± 2	185 ± 1	275 ± 9
50	33 ± 3	87 ± 3	180 ± 5	275 ± 16
71	24 ± 6	71 ± 8	175 ± 5	285 ± 10
110	15 ± 3	46 ± 4	150 ± 5	215 ± 12
140	14 ± 2	-	139 ± 3	265 ± 18
171	28 ± 2	-	111 ± 8	245 ± 26
213	29 ± 3	-	111 ± 20	275 ± 23

Table 4.4: Locations of the peaks A,B,C and D for TiS_xSe_{2-x} ($x = 0.13$) at different temperatures, extracted with a multi-peak fit.

For the ternary compounds TiS_xSe_{2-x}, $x = 0.33$, and $TiTe_xSe_{2-x}$, $x = 0.05$, the CDW

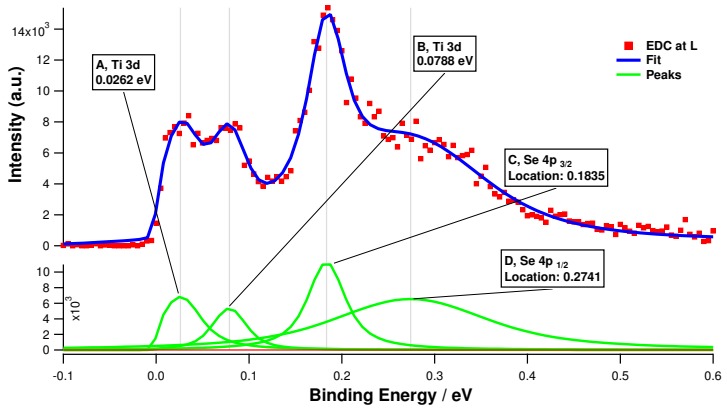

Figure 4.16: EDC of TiS_xSe_{2-x} ($x = 0.13$) at L ($T = 31\,\mathrm{K}$) with multi-peak fit.

phase is much less developed, thus only spectra at low temperature are given here. Figure 4.19 shows spectra for $TiS_{0.33}Se_{1.67}$ (left) and $TiTe_{0.05}Se_{1.95}$ (right) at low temperature around 30 K. The Ti 3*d* emission is quite flat and the backfolded band very weak for the sulphur sample and very weak as well as diffuse for the tellurium sample.

A comparison of the EDCs at L (fig. 4.20) shows that the intensity of the backfolded bands is high for $TiS_{0.13}Se_{1.87}$, which looks very much like the results for $TiSe_2$. However, $TiS_{0.33}Se_{1.67}$ and $TiTe_{0.05}Se_{1.95}$ show a much stronger Ti 3*d* emission and exhibit a shape that is found for a weak CDW phase as seen e.g. for high temperature. The split-off of the Se 4*p* band is not observeable in $TiS_{0.33}Se_{1.67}$ any more. This could be due to the sulphur content, as the splitting is expected to be smaller for an increased sulphur content, see e.g the work of `Albrecht` [64]. Additionally, the spectrum seems to exhibit a shift of 10 meV which could have an experimental cause. The gap between A and C is indeed with 150 meV the smallest for the tellurium sample, while it is growing with an increasing sulphur content, 160 meV for $x = 0.13$ and 180 meV for $x = 0.33$.
To summarize, the results in ARPES for the ternary crystals indicate a less developed CDW phase for $TiS_{0.33}Se_{1.67}$ and $TiTe_{0.05}Se_{1.95}$, while the result for $TiS_{0.13}Se_{1.87}$ is very similar to the one for pure $TiSe_2$. Taking into consideration the size of the band gap, which is 150 meV for $TiSe_2$ and should be around 170 meV for $TiS_{0.13}Se_{1.87}$, one could conclude that the optimal band gap lies between 150 and 170 meV, while 200 meV for $x = 0.33$ already seems to be too big and 100 meV for $TiTe_{0.05}Se_{1.95}$ too small.

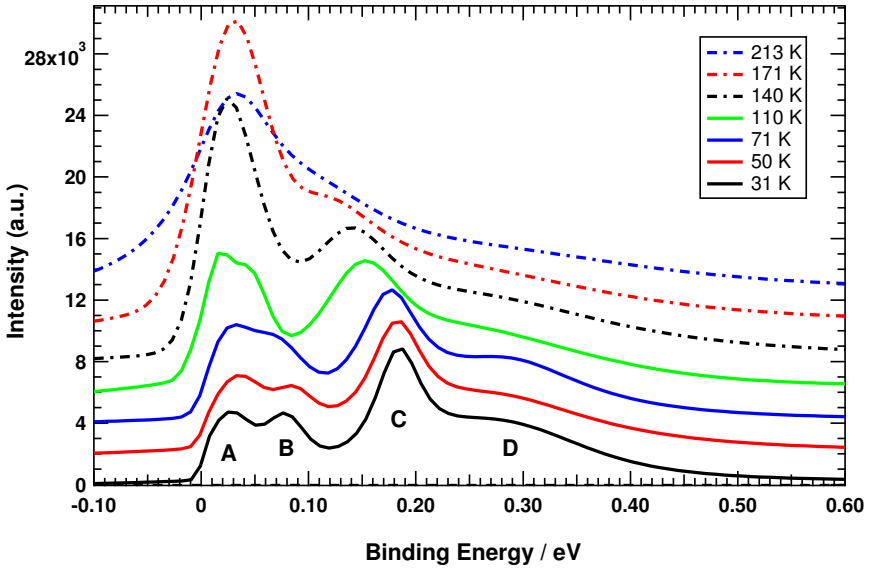

Figure 4.17: Waterfall plot of the fit results at L for different temperatures for $TiS_{0.13}Se_{1.87}$ with peak positions A, B, C, D, normalized to peak C.

Material	A / meV	B / meV	C / meV	D / meV
$TiTe_{0.05}Se_{1.95}$	30 ± 5	-	179 ± 6	280 ± 100
$TiS_{0.13}Se_{1.87}$	25 ± 3	78 ± 4	184 ± 1	272 ± 12
$TiS_{0.33}Se_{1.67}$	21 ± 1	-	200 ± 60	330 ± 100

Table 4.5: Locations of the peaks A,B,C and D for the ternary compounds at low temperature ($T =\simeq 30\,\mathrm{K}$), extracted with a multi-peak fit.

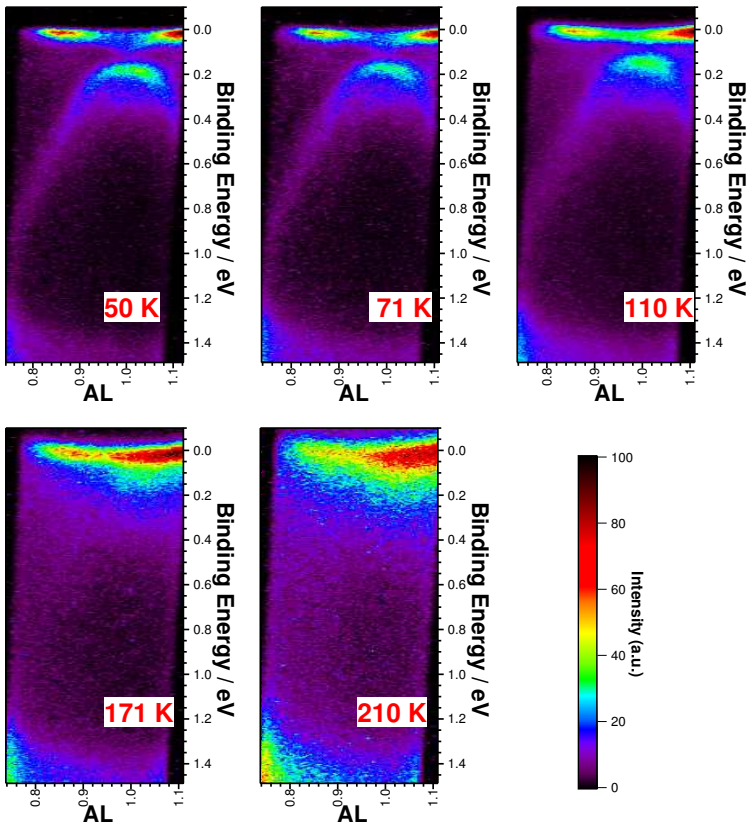

Figure 4.18: Intermediate steps of the temperature evolution of the backfolded bands at L.

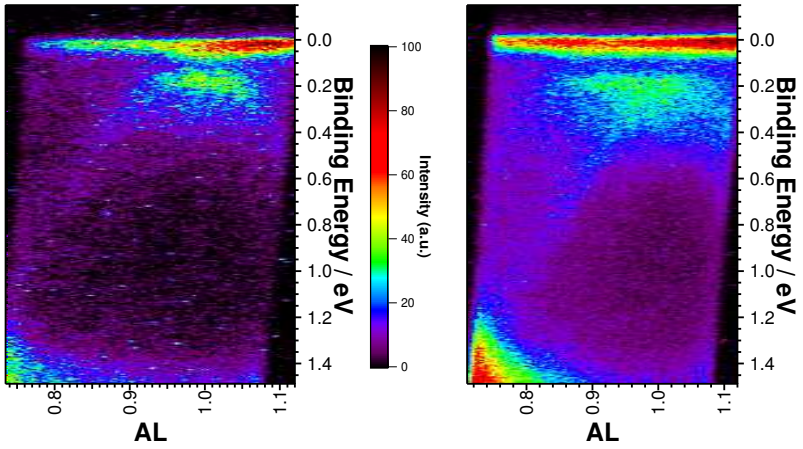

Figure 4.19: Spectra for $TiTe_xSe_{2-x}, x = 0.05$ (left) and $TiS_xSe_{2-x}, x = 0.33$ (right) at $T \simeq 30\,\mathrm{K}$.

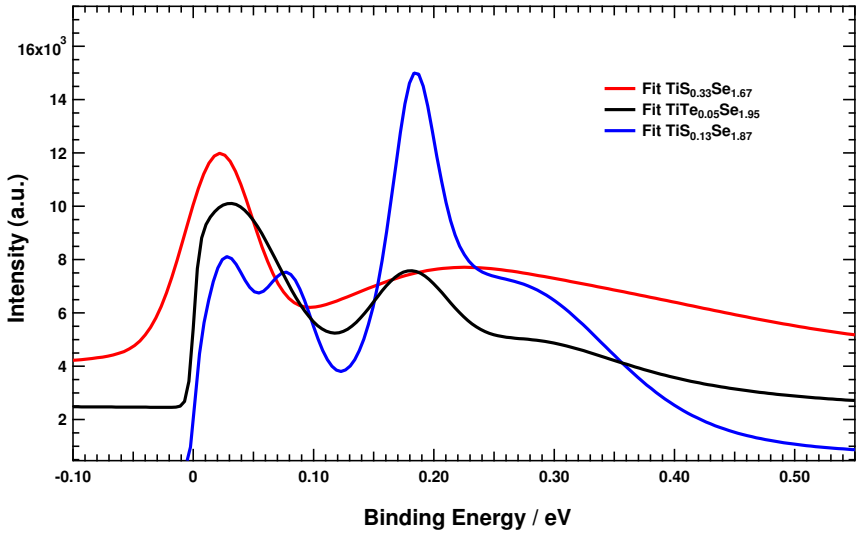

Figure 4.20: Waterfall plot of the evolution of the EDC at L for the different ternary compounds, low temperature $T \simeq 30\,\mathrm{K}$. The graph shows the fits normalized to the uppermost peak around 30 meV.

4.3.5 $TiSe_2$ with H_2O

The influence of water adsorption on the CDW phase in $TiSe_2$ will be described in this section. As the evolution with increasing temperature for a fixed amount of H_2O is similar to the case without water, only spectra at low temperature will be considered here.

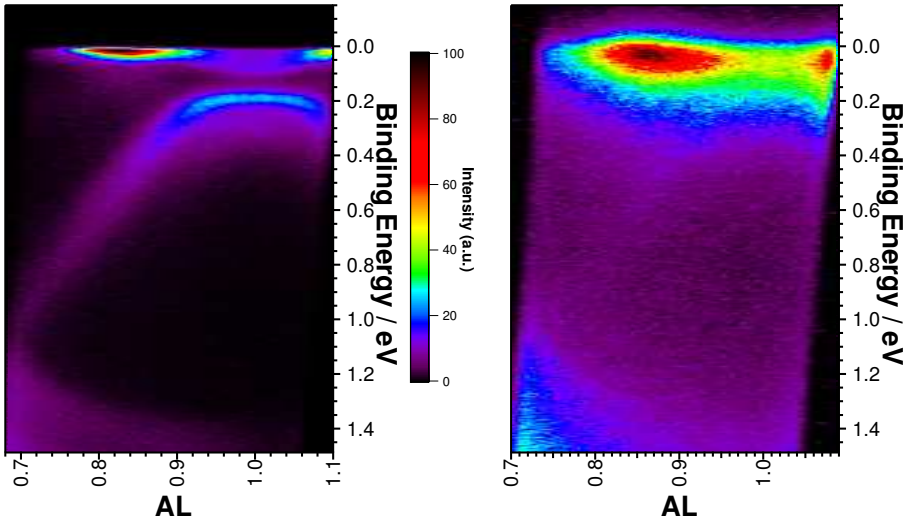

Figure 4.21: Spectra at L without water at 24 K and with 6 kL at 28 K.

Figure 4.21 shows a comparison of a spectrum around L at low temperature before and after the adsorption of 6 kL of water. The backfolded bands can hardly be identified after the water deposition. With only 3.2 kL of H_2O (fig. 4.22) the suppression is much weaker. An analysis of the EDC at L reveals a shape very similar to the shape of the EDC without water but at 140 K. The intensities of the Ti $3d$ and Se $4p_{3/2}$ equal, the peaks A, C and D can be found at the positions 28, 144 and 274 meV for 140 K, while the fit for 3.2 kL (results see tab. 4.6) reveals 40, 149 and 270 meV respectively. Thus the Se peak shifts towards E_F, though the band bending should shift it away: For one monolayer achieved at around 30 kL, the bending of the bands should be around 80 meV [12]. The evolution of the EDC at L with increasing amount of adsorbed water is given in fig. 4.23 with the fit results in table 4.6. Again, the evolution is very similar to the suppression of the CDW phase caused by an increasing temperature.

Hence a rising population of the Ti $3d$ band induced by H_2O band bending gradually suppresses the CDW formation with an evolution very similar to an increasing temperature.

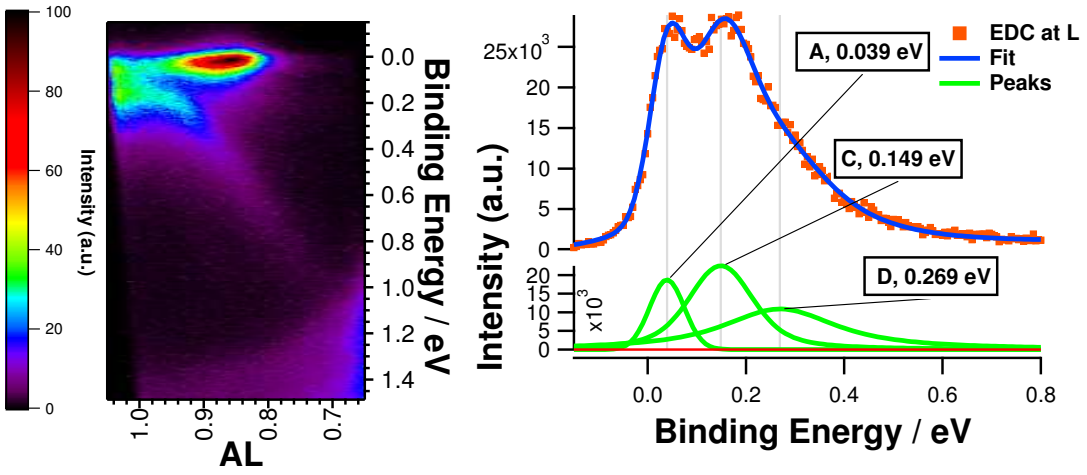

Figure 4.22: Spectrum with 3.2 kL at 22 K (left) and EDC at L (right).

H_2O / kL	A / meV	B / meV	C / meV
3.2	40 ± 2	149 ± 8	270 ± 75
6	44 ± 7	133 ± 15	230 ± 100
10	32 ± 2	143 ± 15	290 ± 150
20	19 ± 2	65 ± 4	184 ± 22

Table 4.6: Locations with fit errors of the peaks A,B,C and D for different amounts of water, extracted with a multi-peak fit.

Third band at A A surprising but reproducible observation was made with 6 kL water at low temperature: Three valence bands instead of two could be suddenly identified at A. Figure 4.24 shows the corresponding spectrum at 40 K with red dots indicating the fitted maxima. The uppermost, almost dispersionless emission just below E_F is partly related to the conduction band bended below the Fermi level as well as a dispersionless emission related to the water, as discussed in detail by `Thürmer` [12]. In order to find out the origin of the third band, the effective masses of the three valence bands A_1, A_2 and A_3 (starting from E_F) were calculated (tab. 4.7). Comparing these results with the results for the bands at A without H_2O (tab. 4.2) does not allow a clear conclusion. But the values for the uppermost band without water, $m^* = 0.16\, m_e$ and energy offset $E_0 = 385$ meV are very similar to the value $A_2 = 0.15\, m_e$ and $E_0 = 365$ found here. However, the band A_1 is shifted 60 meV towards E_F with H_2O ($E_0 = 141$ meV) compared to the value without H_2O ($E_0 = 205$ meV). The effective masses of A_1 and A_3 look very

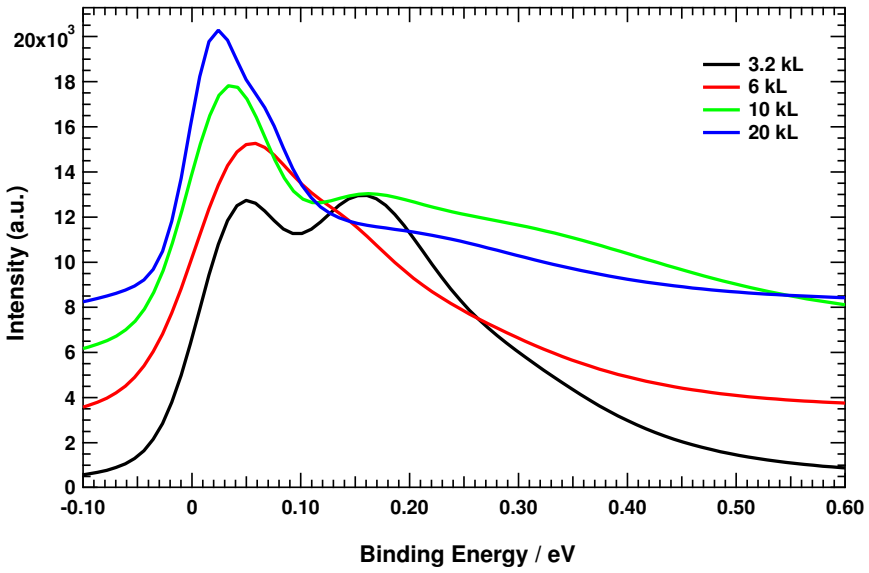

Figure 4.23: Waterfall plot of the evolution of the EDC at L with increasing water adsorption, low temperature $T \simeq 25\,\mathrm{K}$. The graph shows the fits normalized to the uppermost peak around 50 meV.

similar here, but do not have an equivalent for the bands without H_2O. This effect could not be observed for spectra with H_2O at room temperature, so it seems to be a feature of the CDW phase in combination with the water adsorption.
One possible explanation could be that the third band A_3 is a feature of the backfolding in the c-direction. As the superstructure is of type 2x2x2 one gets a new Γ^* point of the superstructure at A. Looking at the theoretical band structure in fig. 2.4, one expects 3 valence bands at Γ near E_F, with the third band at higher binding energies which can also be seen e.g. in experimental results of `Rossnagel et al.` [32]. The results from `Rasch et al.` [4] who found the maximum of the valence band at an energy 40 meV higher for Γ compared to A, fit quite well to the offset of 60 meV found here. The absolute positions of the bands in the CDW phase are however probably not the same as in the normal phase. Hence a suppression of the CDW backfolding in the plane perpendicular to c seems to reveal the backfolding in the third dimension.

4.3.6 Reduced growth temperature

The results of `Di Salvo et al.` [5] indicate a strong dependence of the CDW phase transition on the crystal growth temperature, as shown with resistivity measurements. This was qualitatively confirmed in section 4.2, showing that for a growth temperature

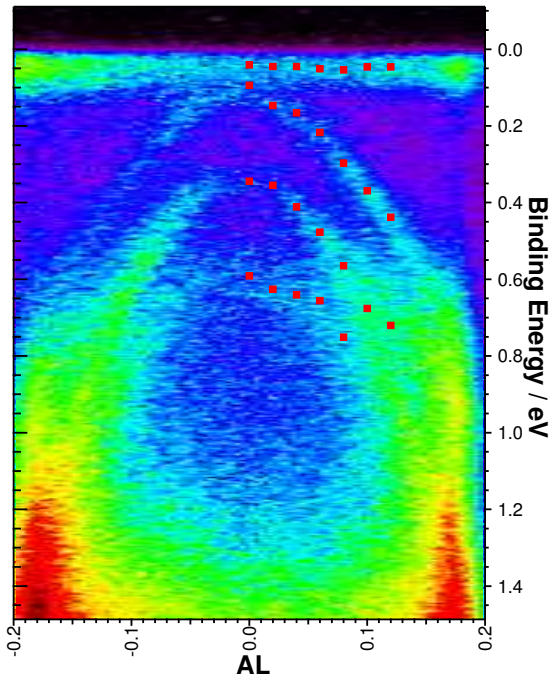

Figure 4.24: Spectrum of the valence bands at A, 6 kL water and $T = 40\,\mathrm{K}$. Red dots indicate fitted maxima.

Band	m_e^*/m_e	E_0 / meV
A_1	0.19 ± 0.02	141 ± 9
A_2	0.15 ± 0.05	365 ± 17
A_3	0.19 ± 0.05	600 ± 12

Table 4.7: Effective masses m_e^* and energy offset E_0 of the bands A_1, A_2, A_3 at A, 6 kL water and $T = 40\,\mathrm{K}$.

$T_g = 630\,^\circ\mathrm{C}$ the resistivity peak is much more pronounced. The ARPES spectrum (fig. 4.25) at low temperature looks indeed different: The Ti $3d$ emission peaks close to L, the strong contribution around 0.8 AL cannot be seen. Furthermore, the backfolded band can be traced to slightly higher binding energies. The EDC at L looks however very much like the EDCs for samples grown at $T_g = 740\,^\circ\mathrm{C}$, but the two contributions of the Ti $3d$ band can hardly be distinguished.

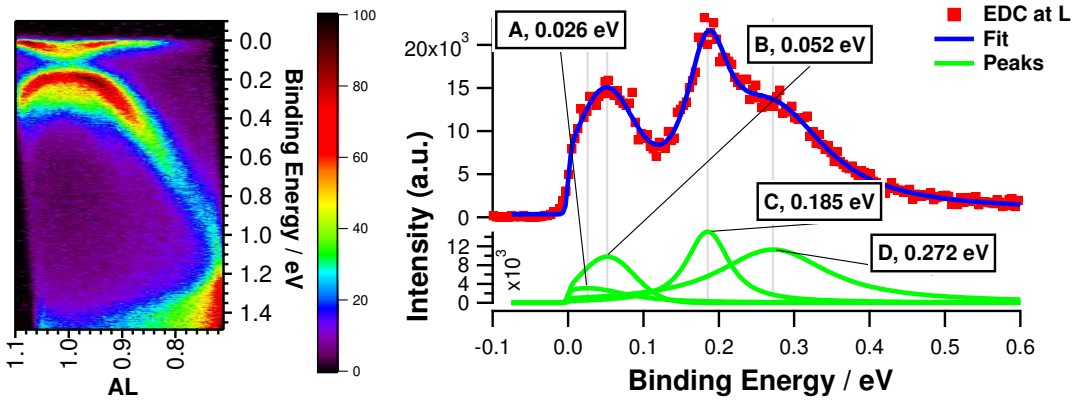

Figure 4.25: Spectrum at L (left, $T = 22\,\mathrm{K}$) and fit (right) for a growth temperature $T_g = 630\,\mathrm{K}$.

4.4 Discussion

The ARPES results for the pure $TiSe_2$ samples at low temperature indicate a well established CDW phase: Two contributions in the Ti $3d$ conduction band can be clearly identified, which is a feature that quickly disappears with the suppression of the CDW by increasing the temperature. This agrees with the results of `Monney et al.` [39] quite well. According to their model the strong peak of the conduction band at 0.8 AL (fig. 4.12) could be related to a backfolded conduction band from another L point, though their experimental results do not show this. These peaks could be another hint for a strong CDW phase. They disappear with increasing temperature before the backfolded valence band disappears (fig. 4.18). A comparison with the samples grown at $T_g = 630\,\mathrm{K}$ (fig. 4.25) shows that they exhibit basically the same features for the EDC exactly at L but that the peaks related to the backfolded conduction band do not appear. If one assumes this as an indicator for the strength of the CDW, the samples with $T_g = 630\,\mathrm{K}$ have a less developed CDW phase. This is supported by the fact that the distinction of two contributions for the conduction band in the EDC at L is clearer for the samples grown at higher temperatures. On the other hand, the traceability of the backfolded valence band to higher binding energies for the samples with lower growth temperatures could be seen as an argument for the strength of the CDW phase. The sum of the arguments seems to support the view that a well-established backfolded conduction band is a good indicator for the CDW strength.

The ternary crystals also show a CDW phase in ARPES. The features of the CDW phase in the spectra of $TiS_{0.13}Se_{1.87}$ are equally well developed compared to $TiSe_2$. Adding more sulphur, $TiS_{0.33}Se_{1.67}$ exhibits a much weaker CDW phase as well as $TiTe_{0.05}Se_{1.85}$. If one assumes that the main difference between the ternary crystals and $TiSe_2$ is the size of the band gap, the optimal gap size seems to lie between 150 meV for $TiSe_2$ and 170 meV (linearly interpolated) for $TiS_{0.13}Se_{1.87}$, whereas 100 meV for $TiTe_{0.05}Se_{1.85}$ is too small and 200 meV for $TiS_{0.33}Se_{1.67}$ too big.

The H_2O adsorption experiments show a gradual suppression of the CDW phase with an increasing amount of water. This water adsorption causes an increased population of the conduction band. A band-type Jahn-Teller that splits and lowers the states in the conduction band actually relies on at least their partial occupation. Hence a partial, additional population by water induced band bending should not instantly lead to a suppression of the CDW phase as excited electrons would find the lowest states in the conduction band already occupied. Yet in the view of an excitonic origin an additional population in the conduction band could hinder the formation of electron-hole pairs. This leads to the conclusion that the H_2O experiments support an excitonic origin of the CDW phase. The appearance of a third band at A (fig. 4.24) for 6 kL cannot be completely explained here, though the positions of the bands indicate a backfolding from Γ as the possible origin. Why this effect only appears at relatively high water adsorption remains unclear.

The classification of the resistivity results turns out to be difficult. The peak in resistivity is much more pronounced for the $TiSe_2$ samples grown at lower temperature and the minimum of its derivative, defined as the critical temperature T_c, can be found at a higher temperature 191 K instead of 163 K for the samples grown at $T_g = 740\,^{\circ}\mathrm{C}$. Both sulphur samples show a reduced T_c of 133 K for $x = 0.13$ and 94 K for $x = 0.33$ whereas a small content $x = 0.05$ of tellurium already suppresses the peak in resistivity completely. This contradicts the photoelectron spectroscopy results indicating a strong CDW phase for $TiS_{0.13}Se_{1.87}$ and a still quite well observable backfolded valence band for the tellurium sample.

An explanation could be that both effects are not as tightly coupled as thought. The excitonic model cannot explain the atomic displacements, while a Jahn-Teller effect lacks an explanation of the strong transfer of spectral weight. A combination of excitonic and phononic Jahn-Teller effect was already proposed by `Wezel et al.` [15]. The phonons could be the cause of the anomaly in resistivity and the periodical lattice distortion. While their occurrence seems to be diminished by the use of higher growth temperatures and by the substitution of selenium with sulphur and especially tellurium, the formation of excitons is not as sensitive to those influences. According to `Di Salvo et al.` [5]

different growth temperatures lead to different levels of doping. Thus one could indeed imagine that the Jahn-Teller effect is more sensitive to the relative position of the Fermi level in the energy gap as it relies on a partial occupation of the conduction band. On the other hand, the excitonic effect could be more sensitive to the actual size of the band gap.

5 Summary

The charge density wave phase transition in $1T-TiSe_2$ has been investigated. To get a more detailed understanding of the CDW phase, $TiSe_2$ as well as the derived ternary compounds TiS_xSe_{2-x} and $TiTe_xSe_{2-x}$ were grown by chemical vapour transport. Those ternary compounds are expected to exhibit a bigger band gap with increasing sulphur content and a smaller band gap for compounds with tellurium. Their CDW phase was probed by means of resistivity measurements as well as angle-resolved photoelectron spectroscopy at the BESSY beamline BEST. The range of the ARPES experiments was extended by the technique of H_2O adsorption investigating the influence of a gradually increased population of the conduction band by H_2O induced band bending.

It was found that the CDW phase probed in ARPES could be gradually suppressed by two influences:

- The substitution of selenium in the ternary compounds with a sulphur content of $x = 0.33$ and a tellurium content of $x = 0.05$.
- An increased population of the Ti $3d$ conduction band induced by H_2O provoked band bending.

The hump in the temperature dependent resistivity, usually regarded as a "fingerprint" of the CDW transition in $TiSe_2$, reveals a strong dependence on the growth temperature being much more pronounced at lower growth temperatures. For the ternary compounds it quickly diminishes with increasing sulphur content and cannot be identified for $TiTe_{0.05}Se_{1.95}$ any more. This is not coherent with the ARPES experiments probing the band structure and making the electronic CDW superstructure directly visible. Thus, the significance of the hump in resistivity for the CDW transition is questioned.

A classification of the presented experiments within the theory could lead to the following conclusion: The H_2O adsorption experiments support an excitonic origin of the CDW phase as an increased population of the conduction band hinders the formation of electron-hole pairs. An increase or decrease of the band gap size for the ternary compounds suggest an optimal band gap between 150 meV for $TiSe_2$ and 170 meV for $TiS_{0.13}Se_{1.87}$. In the context of the resistivity measurements, however, an additional Jahn-Teller effect could be suggested (see e.g. [15] proposing a coupled exciton-phonon driven CDW). The phonons involved in this effect could be the cause of the hump and the

atomic displacements. This additional Jahn-Teller effect seems to be quite independent of the excitonic driving force as the ARPES results suggest.

Further neutron or X-ray diffraction studies of the ternary compounds could provide interesting insights on the influence of selenium substitution on the periodical lattice distortion and could clarify if a possible water intercalation changes the lattice constant in c direction.

Bibliography

[1] R. E. Thorne. Charge-density-wave conductors. *Physics Today*, 49(5):42–47, May 1996.

[2] W. A. Little. Possibility of Synthesizing an Organic Superconductor. *Phys. Rev.*, 134(6A):A1416–A1424, Jun 1964.

[3] E Morosan, HW Zandbergen, BS Dennis, JWG Bos, Y Onose, T Klimczuk, AP Ramirez, NP Ong, and RJ Cava. Superconductivity in CuxTiSe2. *Nat. Phys.*, 2(8):544, 2006.

[4] JCE Rasch, T. Stemmler, B. Müller, L. Dudy, and R. Manzke. 1T-TiSe2: Semimetal or Semiconductor? *Phys. Rev. Lett.*, 101(23):237602, Dec 5 2008.

[5] F. J. Di Salvo, D. E. Moncton, and J. V. Waszczak. Electronic properties and superlattice formation in the semimetal $TiSe2$. *Phys. Rev. B*, 14(10):4321, Nov 1976.

[6] A. Paulheim. Photoemission am ternären Schichthalbleitersystem ZrSxSe2-x. Diploma thesis, Humboldt Universität zu Berlin, 01 2010.

[7] JA Wilson and AD Yoffe. The transition metal dichalcogenides discussion and interpretation of the observed optical, electrical and structural properties. *Advances in Physics*, 18(73):193, 1969.

[8] J. Rasch, T. Stemmler, and R. Manzke. Electronic properties of the semiconductor TiSe2. *Journal of Alloys and Compounds*, 442(1-2):262–264, Sep 13 2007. 15th International Conference on Solid Compounds of Transition Elements, Cracow, Poland, Jul 15-20, 2006.

[9] RH Friend and AD Yoffe. Electronic-Properties Of Intercalation Complexes Of The Transition-Metal Dichalcogenides. *Advances In Physics*, 36(1):1–94, JAN-FEB 1987.

[10] D. L. Greenaway and R. Nitsche. Preparation and optical properties of group IV-VI2 chalcogenides having the CdI2 structure. *Journal of Physics and Chemistry of Solids*, 26(9):1445–1458, 1965.

[11] N. V. Smith and M. M. Traum. Angular-resolved ultraviolet photoemission spectroscopy and its application to the layer compounds Ta$Se2$ and Ta$S2$. *Phys. Rev. B*, 11(6):2087–2108, Mar 1975.

[12] S. Thürmer. Der Einfluss von Wasseradsorption auf die elektronische Struktur der Titan-Dichalkogenide. Diploma thesis, Humboldt Universität zu Berlin, 07 2009.

[13] Yang-Soo Kim, Masataka Mizuno, Isao Tanaka, and Hirohiko Adachi. Electronic Structures and Chemical Bonding of TiX_2 (X=S, Se, and Te). *Japanese Journal of Applied Physics*, 37(Part 1, No. 9A):4878–4883, 1998.

[14] Y. S. Kim, M. Mizuno, I. Tanaka, and H. Adachi. Electronic structure and chemical bonding of TiS2 by cluster calculation. *Material Transaction JIM*, 39(7):709–713, JUL 1998.

[15] Jasper van Wezel, Paul Nahai-Williamson, and Siddarth S. Saxena. Exciton-phonon-driven charge density wave in $TiSe2$. *Phys. Rev. B*, 81(16):165109, Apr 2010.

[16] Alex Zunger and A. J. Freeman. Band structure and lattice instability of Ti$Se2$. *Phys. Rev. B*, 17(4):1839–1842, Feb 1978.

[17] D. W. Bullett. Electronic band structure and bonding in transition metal layered dichalcogenides by atomic orbital methods. *Journal of Physics C: Solid State Physics*, 11(22):4501, 1978.

[18] Ali Hussain Reshak and S. Auluck. Electronic and optical properties of the $1T$ phases of $TiS2$, $TiSe2$, and $TiTe2$. *Phys. Rev. B*, 68(24):245113, Dec 2003.

[19] D. R. Allan, A. A. Kelsey, S. J. Clark, R. J. Angel, and G. J. Ackland. High-pressure semiconductor-semimetal transition in $TiS2$. *Phys. Rev. B*, 57(9):5106–5110, Mar 1998.

[20] F. R. Shepherd and P. M. Williams. Photoemission studies of the band structures of transition metal dichalcogenides. I. Groups IVA and IVB. *Journal of Physics C: Solid State Physics*, 7(23):4416, 1974.

[21] C. H. Chen, W. Fabian, F. C. Brown, K. C. Woo, B. Davies, B. DeLong, and A. H. Thompson. Angle-resolved photoemission studies of the band structure of Ti$Se2$ and Ti$S2$. *Phys. Rev. B*, 21(2):615–624, Jan 1980.

[22] R. Claessen, RO. Anderson, GH. Gweon, JW. Allen, WP. Ellis, C. Janowitz, CG. Olson, ZX. Shen, V. Eyert, M. Skibowski, K. Friemelt, E. Bucher, and S. Hüfner. Complete band-structure determination of the quasi-two-dimensional Fermi-liquid reference compound TiTe2. *Physical Review B*, 54(4):2453–2465, Jul 1996.

[23] M. Moustafa, T. Zandt, C. Janowitz, and R. Manzke. Growth and band gap determination of the $ZrSxSe2 - x$ single crystal series. *Phys. Rev. B*, 80(3):035206, Jul 2009.

[24] C. E. Mortimer and U. Müller. *Chemie.* Thieme, Stuttgart, 8th edition, 2003.

[25] A. H. Thompson. Pauling's Ionicity and Charge-Density Waves in Layered Transition-Metal Dichalcogenides. *Phys. Rev. Lett.*, 34(9):520–524, Mar 1975.

[26] JA Wilson, FJ Disalvo, and S Mahajan. Charge-Density Waves And Superlattices In Metallic Layered Transition-Metal Dichalcogenides. *Advances In Physics*, 24:117–201, 1975.

[27] AF Kusmartseva, B Sipos, H Berger, L Forro, and E Tutis. Pressure Induced Superconductivity in Pristine 1T-TiSe2. *Phys. Rev. Lett.*, 103:236401, 2009.

[28] H. P. Hughes. Structural distortion in TiSe 2 and related materials-a possible Jahn-Teller effect? *Journal of Physics C: Solid State Physics*, 10(11):L319, 1977.

[29] H. Cercellier, C. Monney, F. Clerc, C. Battaglia, L. Despont, M. G. Garnier, H. Beck, P. Aebi, L. Patthey, H. Berger, and L. Forro. Evidence for an Excitonic Insulator Phase in 1T-TiSe[sub 2]. *Physical Review Letters*, 99(14):146403, 2007.

[30] E. Wolfgang Finckh Wolfgang Tremel. Ladungsdichtewellen: Elektrische Leitfähigkeit. *Chemie in unserer Zeit*, 38(5):326–339, 2004.

[31] R. Peierls. Zur Theorie der elektirschen und thermischen Leitfähigkeit von Metallen. *Annalen der Physik*, 4(2):121–148, 1930.

[32] K. Rossnagel, L. Kipp, and M. Skibowski. Charge-density-wave phase transition in $1T - TiSe2$: Excitonic insulator versus band-type Jahn-Teller mechanism. *Phys. Rev. B*, 65(23):235101, May 2002.

[33] TE Kidd, T Miller, MY Chou, and TC Chiang. Electron-hole coupling and the charge density wave transition in TiSe2. *Physical Review Letters*, 88(22):226402, 2002.

[34] D. Jérome, T. M. Rice, and W. Kohn. Excitonic Insulator. *Phys. Rev.*, 158(2):462–475, Jun 1967.

[35] N. F. Mott. The transition to the metallic state. *Philosophical Magazine*, 6(62):287 – 309, 1961.

[36] C. Monney, H. Cercellier, F. Clerc, C. Battaglia, E. F. Schwier, C. Didiot, M. G. Garnier, H. Beck, P. Aebi, H. Berger, L. Forró, and L. Patthey. Spontaneous exciton condensation in $1T$-$TiSe_2$: BCS-like approach. *Phys. Rev. B*, 79(4):045116, Jan 2009.

[37] D. Ihle, M. Pfafferott, E. Burovski, F. X. Bronold, and H. Fehske. Bound state formation and the nature of the excitonic insulator phase in the extended Falicov-Kimball model. *Phys. Rev. B*, 78(19):193103, Nov 2008.

[38] O. Anderson, G. Karschnick, R. Manzke, and M. Skibowski. The phase transition in the electronic structure of 1T-TiSe2. *Solid State Communications*, 53(4):339–342, 1985.

[39] C. Monney, E. F. Schwier, M. G. Garnier, N. Mariotti, C. Didiot, H. Beck, P. Aebi, H. Cercellier, J. Marcus, C. Battaglia, H. Berger, and A. N. Titov. Temperature-dependent photoemission on $1T - TiSe2$: Interpretation within the exciton condensate phase model. *Phys. Rev. B*, 81(15):155104, Apr 2010.

[40] A. Spijkerman, JL. de Boer, A. Meetsma, GA. Wiegers, and S. van Smaalen. X-ray crystal-structure refinement of the nearly commensurate phase of $1T - TaS_2$ in $(3 + 2)$-dimensional superspace. *Phys. Rev. B*, 56(21):13757–13767, Dec 1997.

[41] John A. Wilson. Concerning the semimetallic characters of TiS2 and TiSe2. *Solid State Communications*, 22(9):551–553, 1977.

[42] T Pillo, J Hayoz, H Berger, F Levy, L Schlapbach, and P Aebi. Photoemission of bands above the Fermi level: The excitonic insulator phase transition in 1T-TiSe2. *Physical Review B*, 61:16213–16222, 2000.

[43] H. Schäfer, H. Jacob, and K. Etzel. Über den Transport des Bodenkörpers im Temperaturgefälle mit Hilfe heterogener Gleichgewichte. *Zeitschrift für anorganische und allgemeine Chemie*, 286(1-2):27–41, 1956.

[44] H. Schäfer. *Chemische Transportreaktionen.* Verlag Chemie, Weinheim, 1962.

[45] H. Stöcker. *Taschenbuch der Physik.* Verlag Harri Deutsch, Frankfurt am Main, 4th edition, 2000.

[46] R. Nitsche. The growth of single crystals of binary and ternary chalcogenides by chemical transport reactions. *Journal of Physics and Chemistry of Solids*, 17(1-2):163–165, 1960.

[47] J. Augustin. *Der elektronische Übergang unmodulierter zu modulierten Schichtkristallen - Bandstrukturen und CDW-Phaseneffekt.* dissertation, Humboldt-Universität zu Berlin, 2005.

[48] E. Preuss, B. Krahl-Urban, and R. Butz. *Laue Atlas*. Bertelsmann Universitätsverlag, Düsseldorf, 1971.

[49] H. Hertz. Ueber einen Einfluss des ultravioletten Lichtes auf die electrische Entladung. *Annalen der Physik und Chemie*, 267(8):983–1000, 1887.

[50] A. Einstein. Über einen die Erzeugung und Verwandlung des Lichtes betreffenden heuristischen Gesichtspunkt. *Annalen Der Physik*, 17(6):132–148, Jun 1905.

[51] L. Dudy. *Nature and organization of the CuO2-plane*. Dissertation, Humboldt-Universität zu Berlin, 2008.

[52] Stefan Hüfner. *Photoelectron Spectroscopy*. Springer, 3rd edition, 2003.

[53] J. Végh. The Shirley background revised. *Journal of Electron Spectroscopy and Related Phenomena*, 151(3):159–164, 2006.

[54] J Braun. The theory of angle-resolved ultraviolet photoemission and its applications to ordered materials. *Reports On Progress In Physics*, 59:1267–1338, 1996.

[55] Bessy website, www.bessy.de.

[56] M. Kreier. http://people.physik.hu-berlin.de/ kreier/.

[57] T. Zandt, C. Janowitz, and R. Manzke. Status of 5m-NIM Beamline. *BESSY - Annual Report*, pages 225–227, 2006.

[58] T. Zandt, L. Dudy, C. Janowitz, and R. Manzke. The new Photoemission Endstation at the Beamline for Education and Scientific Training (BEST). *BESSY - Annual Report*, pages 283–285, 2007.

[59] PREVAC Ltd. *ARPES-System BEST - Technical manual*.

[60] J. Rasch. Water Adsorption on $1T$-$TiSe_2$ Surfaces probed with Angle Resolved Photoemission Spectroscopy. Diploma thesis, Humboldt-Universität zu Berlin, 2006.

[61] G. Karschnick, O. Anderson, W. Drube, and M. Skibowski. Adsorbate enhanced Ti-3d photoemission from layered TiSe2 surfaces. *Surface Science*, 155(1):46–52, 1985.

[62] C. Brabetz. Charakterisierung von Hochtemperatur-Supraleitern. Bachelor's thesis, Humboldt-Universität zu Berlin, 2008.

[63] C. Brabetz. Zum Einfluss des Dotierens auf den CDW-Phasenübergang in $TiSe_2$. Master's thesis, Humboldt-Universität zu Berlin, 04 2010.

[64] W. Albrecht. Band structure analysis and work function determination of ternary compounds in the series ZrS_xSe_{2-x}. Bachelor's thesis, Humboldt-Universität zu Berlin, 8 2010.

List of Figures

List of Tables

List of abbreviations

ARPES	Angular Resolved Photoelectron Spectroscopy
BESSY	Berliner Elektronenspeicherring-Gesellschaft für Synchrotronstrahlung
BEST	Beamline for Education and Scientific Training
BCS	Bardeen Cooper Schrieffer
CDW	Charge Density Wave
CVT	Chemical Vapour Transport
EDC	Energy Distribution Curve
EDX	Energy-Dispersive X-ray Spectroscopy
EES	Arbeitsgruppe Elektronische Eigenschaften und Supraleitung
HU	Humboldt-Universität zu Berlin
LEED	Low Energy Electron Diffraction
NIM	Normal Incidence Monochromator
PES	Photoelectron spectroscopy
PID	Proportional-Integral-Derivative
PLD	Periodical lattice distortion
TMDC	Transition Metal Dichalcogenide
TMP	Turbo Molecular Pump
UHV	Ultra-High Vacuum

Acknowledgements

I would like to thank

- Prof. Manzke for enabling this thesis in an exciting field of condensed matter physics
- Dr. Janowitz for interesting problem discussions
- Christine Brabetz for the excellent teamwork and the pickled apples at BESSY night shifts
- Beate Müller for helpful discussions as well as the Laue pictures
- Dr. Dwelk for his support with the transport measurements, Mrs. Kaiser for her assistance with the crystal growth and Mr. Schmidt for technical assistance
- all members of EES
- Jérôme Roy and Jörg Zegenhagen for enabling an internship at ESRF where I could gain first experiences in surface science
- all proofreaders for their effort
- my family for supporting my studies

and especially Kira for her wonderful support, a constant source of motivation.